Title
NANOSCALE FUNCTIONALIZATION OF SOFC CATHODE SURFACE AND INTERFACES

Author
karimaghaloo, alireza

Publication Date
2020

Peer reviewed|Thesis/dissertation

UNIVERSITY OF CALIFORNIA, MERCED

NANOSCALE FUNCTIONALIZATION OF SOFC CATHODE SURFACE AND INTERFACES

by

Alireza Karimaghaloo

A dissertation submitted in partial satisfaction of the
requirements for the degree of
Doctor of Philosophy

in

Mechanical Engineering

Committee in charge:
Dr. Min Hwan Lee, Chair
Dr. Abel Chuang
Dr. James Palko

The dissertation of Alireza Karimaghaloo is approved:

Min Hwan Lee, Chair	Date
Abel Chuang	Date
James Palko	Date

University of California, Merced

Dedicated to my parents who have been a great source of inspiration and support

ACKNOWLEDGEMENTS

Firstly, I would like to express my utmost gratitude to my advisor Professor Min Hwan Lee for the continuous support, patience, motivation, and immense knowledge. Besides my advisor, I would like to thank the rest of my thesis committee, Professor Abel Chuang and Professor Jamez Palko for helping me in this life changing event. And last but not least, I want to thank my fiancé Denette for all her support in this path.

ABSTRACT

Title: NANOSCALE FUNCTIONALIZATION OF SOFC CATHODE SURFACE AND INTERFACES
Author: Alireza Karimaghaloo
Degree: Doctor of Philosophy
University of California, Merced

Committee in charge:
Dr. Min Hwan Lee, Chair
Dr. Abel Chuang
Dr. James Palko

In SOFCs, we observe that the porous electrodes tend to agglomerate and thus decrease the cell performance over time. The agglomeration (or sintering) of a porous oxide can be understood as the diffusion of the oxide atoms along the surface of a material to minimize the surface energy of the structure. Therefore, even an ultrathin overcoat is expected to deter the sintering process and thus maintain the porous geometry for longer period of time. In this thesis, the actual role of YSZ overcoat in the ORR process is presented through a series of electrochemical analyses. Without an overcoat, a nanoporous Pt is significantly agglomerated during a high-temperature operation, and ORR kinetics becomes limited by the availability of TPB. An ultrathin YSZ overcoat significantly suppressed the sintering kinetics and preserved the morphology of its underlying Pt layer. More importantly, the overcoat acts as an excellent facilitator of the atomic oxygen species-mediated chemical process(es), which used to be rate-limiting in the ORR of a non-coated Pt/YSZ system.

In the next step, to understand the impact of spincoated layer on the interface of cathode/electrolyte, EIS data obtained at different temperatures and oxygen partial pressures. Beside SEM imaging and XRD, to support the hypothesis of ORR kinetics, infiltration and ALD coating also performed on different samples. We found out that spincoated layer has smaller nanoparticle sizes and 3~4 times smaller nanocrystalinity that

increase the active cites for dissosiative adsorption on the cathode side, comparing to the available cites on bare LNF. EIS data along with ALD coating also strongly support the hypothesis that ion conducting pass through the LNFGDC FL playes an important role in decreasing the polarization resistance comparing the bare LNF cathode as well. It helps the available cites not limited to the vicinity of GDC interlayer but be available in entire FL and the ion transport to the GDC interlayer through GDC nanoparticles paths.

To sum up, a combination of nanoscale treatments including cathode infiltration, metal oxide ALD coating, and cathode-electrolyte interface spin-coating pursued to achieve a significantly enhanced performance and durability by addressing the issues. In addition, I also performed a systematic studies on the change in electrochemical kinetics and a possible shift of bottleneck process by the treatments to better understand the effect of each of this nano-functionalization on oxygen reduction catalysis process in SOFCs.

TABLE OF CONTENTS

LIST OF FIGURES

LIST OF TABLES

SYMBOLS

$\mathbf{Z}$	impedance
$\mathbf{Z_{real}}$	real component of impedance
$\mathbf{Z_{imag}}$	imaginary component of impedance
$\mathbf{R_{ohm}}$	ohmic resistance
$\mathbf{Z_{fA}}$	anodic polarization resistance
$\mathbf{R_p}$	cathodic polarization resistance
$\mathbf{R_{ct}}$	charge transfer resistance
L	inductor circuit element
Q	constant phase circuit element
R	resistor circuit element or resistance
t	thickness
A	cross sectional area
σ	conductivity
Ω	resistance
V(t)	voltage function
i(t)	current function
φ	phase shift/phase angle

ABBREVIATIONS

ALD	atomic layer deposition
ASR	area-specific resistance
BSCF	$Ba_{0.5}Sr_{0.5}Co_{0.8}Fe_{0.2}O_{3-\delta}$
CCL	current collecting layer
CTE	thermal expansion coefficient
CVD	Chemical Vapor Deposition
EIS	electrochemical impedance spectroscopy
FEG	field emission gun
FL	functional layer
GDC	$Gd_{0.1}Ce_{0.9}O_{2-\delta}$
HOR	hydrogen oxidation reaction
HT-SOFC	high-temperature solid oxide fuel cell
IT-SOFC	intermediate temperature solid oxide fuel cell
LSCF	$(La_{0.6}Sr_{0.4})_{0.95}Co_{0.2}Fe_{0.8}O_{3-\delta}$
LSCo	$La_{0.8}Sr_{0.2}CoO_3$
LSF	$La_{0.8}Sr_{0.2}FeO_3$
LSGM	$La_{0.8}Sr_{0.2}Fe_{0.83}Mg_{0.17}O_{2.815}$
LSM	lanthanum strontium manganite
LT-SOFC	low-temperature solid oxide fuel cell
MIEC	mixed ionic/electronic conductor
OCV	open-circuit voltage
ORR	oxygen reduction reaction
PBC	$PrBaCo_2O_{5+\delta}$
PEM	proton exchange membrane
sccm	standard cubic centimeters per second
SEM	scanning electron microscope
SOFC	solid oxide fuel cell
SSC	$Sm_{0.5}Sr_{0.5}CoO_{3\delta}$
SScC	$SrSc_{0.2}Co_{0.8}O_{3-\delta}$
TPB	Triple phase boundary
XPS	x-ray photoelectron spectroscopy
YDC	yttrium-doped ceria
YSZ	yttrium-stabilized zirconia

Chapter 1 Introduction

1-1 Fuel cells

According to the energy information administration (EIA), in 2018, an American household consumes an average of 10,972 kilowatt-hours (kWh) of electricity per year. Thus, an advantageous approach to energy sustainability is to provide engines that transform the chemical form of energy into the electrical form. One of the best solutions for an electrochemical engine is fuel cells. They directly do the energy transformation without having any intermediate steps. One advantage of the electrochemical engine is that it can use different types of fuels; hydrogen, alcohol or natural gas, and it does not rely on just one type of fuel. The electrochemical engine creates flexibility in terms of finding a source of energy. Another advantage of using electrochemical devices is that they are eco-friendly since they do not burn the fuels and directly convert chemical to the electrical form of energy, so it not only limits the emission of greenhouse gases but also increases the efficiency by reducing the heat waste that happens during the burning process.[1]

The theoretical concept of fuel cell offered by Davy[2] was carried forward by Grove[3] to make it a reality in earlier decades of the 19th century. In Grove's cells, the reaction of H_2 and O_2 leads to the formation of water. It was just towards the end of the 19th century in which a solid material was used as an electrolyte by Nernst[4] in his device 'glower'. This concept leads to the demonstration of the SOFC by Baur and Preis[5] during the first half of the 20th century. The need for efficient energy conversion has increasingly driven research in fuel cells. In the 1960s, the use of fuel cells was limited to spacecraft and submarines. During the 1980s, we had huge improvement in material technology and characterizations led to renewed research interests on fuel cells.

A fuel cell consists of three components. An electrolyte layer through which only ions can pass through and two porous electrodes on both sides of it. The electrode where air or

oxygen is provided is the cathode where oxygen reduction reaction (ORR) occurs, and the electrode on the fuel side is the anode where hydrogen oxidation reaction (HOR) occurs. Most of the time, fuel cells are classified by their type of electrolyte[6] The following lists some of the representative fuel cells:

- Polymer electrolyte fuel cell (PEFC); also known as proton exchange membrane (PEM) fuel cell
- Phosphoric acid fuel cell (PAFC)
- Molten carbonate fuel cell (MCFC)
- Solid oxide fuel cell (SOFC)

1-2 Solid oxide fuel cells

One of the most representative types of fuel cells is SOFCs. Compared to other fuel cells, SOFCs are advantageous in energy conversion efficiency, fuel flexibilities, and the possibility of recovering high-quality exhaust heat for cogenerating power.[4]

SOFCs can be categorized by the shape of a solid oxide material as the electrolyte: circular and planar. Fig. 1-1 shows a schematic diagram of a typical planar SOFC with main functional elements. The SOFC is comprised of two porous electrodes separated by a dense and gas-tight electrolyte. The electrodes must conduct electrons and preferably also oxygen ions, whereas the electrolyte should allow the conduction of oxygen ions only.

Oxygen gas supplied at the cathode is reduced to oxygen ions. They migrate through the electrolyte to the anode, where the fuel, e.g., H_2 or hydrocarbons, is electrochemically oxidized. This reaction releases electrons, which will travel to the cathode through an external circle.

High-temperature SOFCs (HT-SOFC) require high operative temperatures (up to 1200 °C) to permit efficient oxygen ion (O^{2-}) transport. There is a recent shift to use intermediate temperature (IT; 600 – 800 °C) or low temperature (LT; < 600 °C) SOFCs

instead but, there are essential challenges in the kinetics of oxygen ion-conductivity in the electrolyte and electrochemical reactions, in particular of ORR, at lower temperatures.

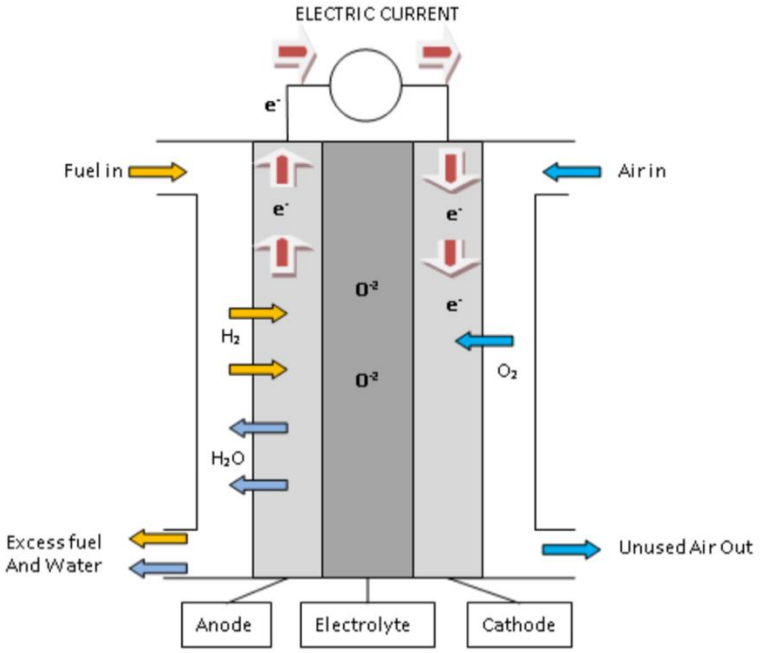

Fig. 1-1 Scheme of a planar SOFC operated with hydrogen and air [1]

Since SOFCs are operated at higher temperatures compared to other types of fuel cells, there are several advantages and disadvantages associated with it including reduced poisoning effect from CO, the use of non-precious metals (thus cheaper materials) as their electrodes, faster cell kinetics, and fuel flexibility. However, there are some disadvantages that the most important one is the limitation of SOFC applications to a few choices such as stationary power plant units, due to the high operative temperature of HT-SOFCs [2].

State-of-the-art SOFCs are used for stationary applications in high power range and operation at temperatures from 800 °C to 1000 °C. The widespread commercialization of SOFCs has remained a challenge, mainly due to the cost and reliability of these devices. The development of IT-SOFCs, operating at 600-800 °C, has been one of the main goals in recent studies. Cost competitiveness can be realized by the use of inexpensive metal supports. Moreover, the lifespan of the cell is expected to increase as the thermal

degradation problems are lessened. LT-SOFCs operating below 500 °C and down to as low as 350 °C are promising power sources for portable electronic devices with power requirements between 1 to 20 W[10], [11]. However, the challenge is in advanced packaging that fulfills complex thermal requirements.[11]

1-2-1 SOFC components

The main parts in each SOFC cell are electrolyte, anode, cathode. Zirconia doped with 8-10 mole % yttria (YSZ) is the most effective electrolyte for HT-SOFCs. Although several other materials have been investigated including Bi_2O_3, CeO_2, and Ta_2O_5[12], zirconia is highly stable in both reducing and oxidizing environments. O^{2-} conduction occurs through the fluorite crystal structure of zirconia in which some of the Zr^{4+} ions are replaced by Y^{3+} ions. When doped with trivalent cation, oxygen sites become vacant to maintain the charge neutrality. Oxide ion transport occurs between vacancies located at tetrahedral sites in the perovskite lattice [13], [14].

Among the SOFC components, the porous anode provides electrochemical reaction sites for the oxidation of the fuel. This porous structure allows fuel and byproducts to be delivered and removed from the anode surface boundaries. It also provides a path for electrons to be transported from the electrolyte/anode reaction sites to the interconnector structure in SOFC stack. Porous Ni/YSZ cement is currently the most common anode material because of acceptable thermodynamic stability and desirable electrochemical properties [15].

Catalytic activity for oxygen reduction and compatibility with the electrolyte are important properties of SOFC cathodes. Chemical stability is one of the important parameters to choose SOFC meterials since SOFCs traditionally operate at high temperetures.Thus, lanthanum manganite-based ceramics, which are one of the best pervskite materials to address the chemical stability are a good choice for SOFCs that operate above 1000 °C. For lower cell operation temperatures, composite cathodes made from LSM/YSZ are used [16]. Moreover, Sr/Co-doped lanthanum ferrites have been widely investigated [17].

Interconnector's main function is to perform as a current-collector and deliver the electrical connection between the different single cells in the stack of fuel cells. Thus, interconnectors need to be highly electron conductive and thermally stable in both anode and cathode cides since the temperature of gases at their operation condition in traditional SOFCs are between 650 –1000 °C, and the thermal expansion coefficient (CTE) similar to that of the ceramic components in anode and cathode sides. Ceramic materials based on La-chromite have shown to possess the property combination required for interconnectors. Recently, there is more attention given on metals as a promising replacements for the La-chromite, particularly for SOFC design, where the interconnect must additionally supply the mechanical support for the thin ceramic parts, and it also should be a gas-proof separation between fuel gas and oxidant. The main reason for this replacement is because they have several advantages over ceramic materials. Metals are easier and cheaper to manufacture than ceramics. They are less fragile, machinable, and can be weld easily while not possible for ceramics. In addition, matals have higher electrical and thermal conductivities than most ceramics.[18]

1-2-2 Cell configuration and stack design

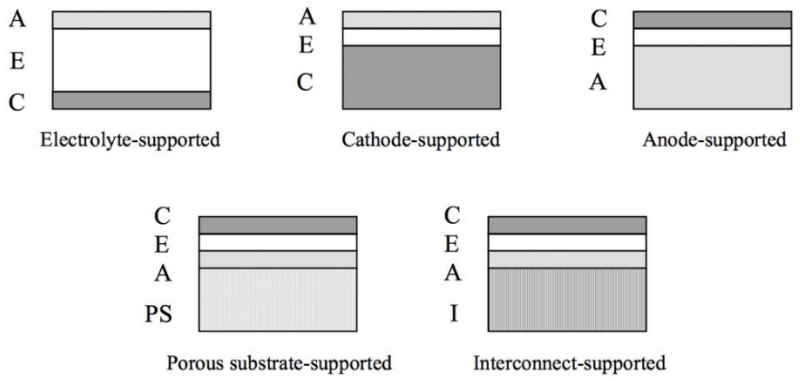

Fig. 1-2 SOFC single-cell configuration [19]

The configurations in SOFC single cell can be classified into two categories: self-supporting cells that one of the cell components, often the thickest one, acts as the cell structural support, and external-supporting cell, which is configured as thin layers on the interconnector a porous outer substrate [2]. Different cell components in several types of cell configurations for SOFCs are schematically demonstrated in Fig. 1-2.

Each single cell (anode, electrolyte, cathode) is connected to the next single cell with the interconnect plate. The group of connected cells is called the SOFC stack. At present, two main designs of the stack have been proposed and developed: tubular and planar design [3](Fig.1-3). In the tubular design, the cell is configured as a tube, and stacks consisting of a pack of single-cell tubes. In the most common tubular design, the tube is made of the cathode material (cathode-supported) and closed at one end. Electrolyte and anode layers are formed on the outside of the tube. In the planar design, the cell is configured as flat plates, which are connected in electrical series. All types of cell configurations (self-supporting or external-supporting) that showed in Fig.1-2 have been considered for the planar design [19].

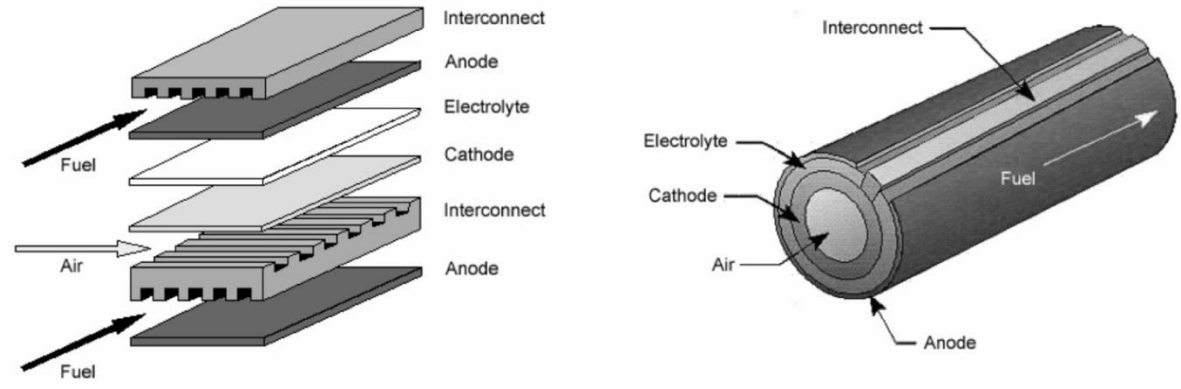

Fig.1-3 SOFC - planar and tubular design [2]

1-2-3 Electrolyte

Electrolyte in SOFCs as it is clear from their name, is made of solid ceramic oxides. The electrolyte sandwiched between the cathod and anode in an SOFC conducts oxygen ions. The main role of the electrolyte layer is to transport O^{2-} ions from the cathode to anode side of the cell. It also plays a mechanical support role in electrolyte supported SOFCs. The electrolyte in SOFCs need to have some important characteristics. First and most important, the material should exhibit high ionic conductivity and negligible electronic conductivity at the same time. In electrolyte supported SOFCs, due to the considerable thickness of the electrolyte, the majority of loss comes from the ohmic resistance corresponding with the oxygen ions flow from cathode side to the anode side through the electrolyte.[8] Thus, the electrolyte material should be as ionically conductive as possible. Chemical stability is also important so the ionic conductivity does not decrease through the cell life time. Since any electrons shorting through the electrolyte will cause a voltage loss in the cell, an excellent SOFC electrolyte should also be insulating against electron conductivity. Ionic flow also have an strong correlation with the thickness of the electrolyte layer. The following equation gives the ohmic resistance of the electrolyte material:

$$R = \frac{t}{\sigma A} \qquad \text{Eq. 1-1}$$

Here, t is the electrolyte thickness, σ is the ionic conductivity, and A is the cross-sectional area. Eq. 1-1 shows that the ohmic resistance of the electrolyte increases linearly with layer thickness, therefore, a thin electrolyte layer to minimizes resistance is essential for optimal performance. However, an excessively thin electrolyte will allow electrons to short through the electrolyte. Studies have shown that an optimal electrolyte thickness of around 15 μm will minimize ohmic resistance while preventing voltage losses due to electron shorting [20]. This thickness can be minimized to a few hundred nanometers by using advanced coating techniques such as atomic layer deposition (ALD). In addition to optimal layer thickness, a SOFC electrolyte should also be as dense as possible, as a porous

electrolyte results in the fuel mixing with the oxidant, which severely decreases the reversible voltage of the cell.

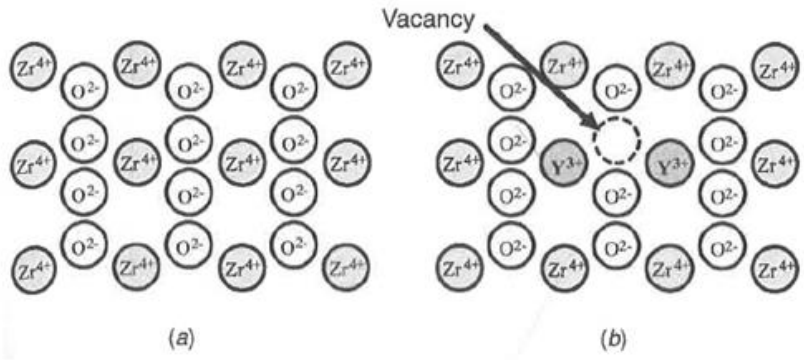

Fig. 1-4 Oxygen vacancies created by doping zirconia with yttria [8]

Chemical and mechanical stability is another requirement for SOFC electrolyte materials. The electrolyte must be able to withstand the high-temperature reducing environment of the anode as well as the high-temperature oxidation environment of the cathode without experiencing any physical or chemical instability. The electrolyte should also be chemically inert so that reactions between the electrolyte and electrodes do not occur. Reactions occurring between the electrolyte and either electrode could lead to a highly resistive phase forming in the electrode-electrolyte interlayer, which dramatically decreases the cell performance [10].

Additionally, the electrolyte will experience mechanical stress due to a mismatch in thermal expansion between electrolyte and electrodes. Therefore, electrolyte materials must have sufficient mechanical strength to resist this stress, particularly for electrolyte supported cells that rely on a relatively thick electrolyte layer for mechanical stability. Finally, material and fabrication costs are substantial barriers to the mass commercialization of SOFC technology. Therefore, SOFC electrolytes should be relatively inexpensive to manufacture.

YSZ is the most widely used SOFC electrolyte material [7] and is the primary electrolyte used for this study. YSZ is fabricated by doping a zirconia backbone (ZrO_2) with yttria molecules (Y_2O_3), resulting in a fluorite crystal structure. During the doping process, yttrium cations (Y^{3+}) diffuse into the zirconia host material and replace zirconium cations (Zr^{4+}) in the crystal lattice. Because of the charge difference between the cations, one oxygen vacancy (O^{2-}) is created each time two yttrium cations replace two zirconium cations in the lattice, so that charge balance is maintained. This is illustrated in Fig. 1-4, which shows the undoped zirconia host, while Fig.1-4b shows an empty O^{2-} a site created by replacing two Zr^{4+} cations with two Y^{3+} cations. These oxygen vacancies are what give YSZ its ionic conductivity as oxygen ions created at the cathode "hop" from one empty O^{2-} site to the next until they reach the anode. Increasing the amount of yttria doping increases the number of empty O^{2-} sites in the lattice, therefore increasing the ionic conductivity. However, there exists an upper limit to doping concentration, beyond which O^{2-} sites begin to interact with one another, and ionic conductivity decreases. Studies have shown that a doping concentration of 8 mol% Y_2O_3 is optimal for the ionic conductivity of YSZ, as shown in Fig. 1-5a [8].

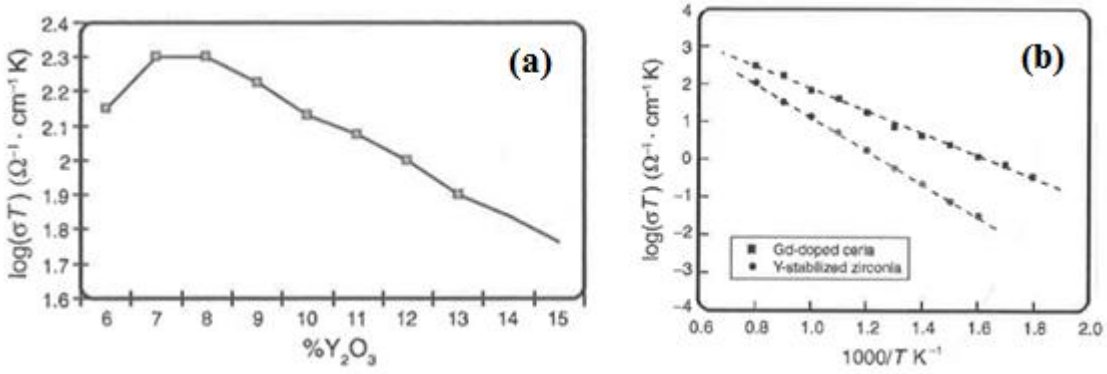

Fig. 1-5 (a) Ionic conductivity vs yttria doping concentration for YSZ; (b) Ionic conductivity vs temperature for YSZ and GDC [8]

Although YSZ is the primary electrolyte material used in this study, gadolinium-doped ceria (GDC) also plays a vital role and will be briefly introduced here. At

temperatures above about 800 °C, YSZ reacts with $(La_{0.6}S_{0.4})_{0.95}Co_{0.2}Fe_{0.8}O_{3-\delta}$ or LSCF to form $SrZrO_3$, an ionically insulating phase which dramatically impedes cell performance. A thin (~5 μm) layer of GDC can be placed between the YSZ electrolyte LSCF cathode to prevent insulating phase formation from occurring during electrode sintering [11]. Furthermore, Like YSZ, GDC exhibits a fluorite crystal structure and shares the same "ion-hopping" mechanism to facilitate ionic conductivity in the electrolyte. However, because the gadolinium dopant ions are similar in size to the host cerium ions, ceria can be doped with a higher concentration of dopant of up to 10-20% compared to the 8 mol% for YSZ. Therefore, GDC generally shows a higher ionic conductivity than YSZ, as Fig. 1-5b, which shows the ionic conductivity as a function of temperature for these materials. However, GDC has several disadvantages compared to YSZ, which is why YSZ is the primary electrolyte used in this study. Firstly, GDC displays significant electronic conductivity in the high temperature reducing environment of the anode, which leads to a dramatic decrease in available open circuit operating voltage and, thus, a decreased overall power density.

Additionally, GDC shows significant chemical expansion when exposed to a reducing environment, causing mechanical failure and delamination inside electrolyte.[8] Therefore, while YSZ is the primary electrolyte material used in this study, a thin layer of GDC is inserted to separate the YSZ electrolyte from the cathode to prevent ionically insulating phases from forming between the YSZ electrolyte and the cathode. Also, it helps adhesion by matching electrolyte and cathode thermal expansions.

1-2-4 Cathode

The cathode in the SOFC is the positive electrode where a reduction reaction of air/oxygen occurs. The oxygen molecules in the oxidant gas get reduced at the cathode-electrolyte interface in standard cathode materials by the electrons in the external circuit. The oxygen ions so produced are transported through the bulk of the electrolyte following the ionic conduction mechanism. To understand the cathode loss to the overall cell loss, one must know the reaction kinetics involves in the reduction process. The exact reaction mechanism of the entire process is complicated and involves some elementary steps. The

reaction mechanism also depends on the type of cathode material (electronic conducting or mixed conducting) used or the pathway of reaction. The reaction fragments, in general, are the surface diffusion, adsorption, dissociation, and transport of oxide ions [20],[17].

Mixed ionic electronic conducting (MIEC) cathode materials allow the bulk transport of the intermediate oxygen species, thereby extend the reaction zones over the entire electrode surface. In other simple cases (cathode materials having electronic conductivity only), the reaction sites are limited to the triple-phase boundary (TPB) only. Thus, the length of the TPBs and the extent of TPBs in MIECs are crucial in determining cathode performance. The length of the TPBs can be enhanced by tailoring the microstructure of the cathode. Taking into account the roles and working of the cathode in SOFC as discussed above, a cathode material should have the following qualities [17],[21]:

- It must be an excellent electronic as well as an adequate ionic conductor.

- It must have excellent chemical and thermal stability under reducing atmosphere at high temperature.

- It must be compatible with the other cell components such as electrolyte and the interconnect.

The state of the art material for SOFC cathode is Sr-doped $LaMnO_3$ [21]. $La_{1-x}Sr_xMnO_{3-\delta}$ (LSM) [22], [23] is used as cathodes in HT-SOFCs. The intensive research and investigation on the cathode materials in the recent decades has produced a wide variety of other options for the cathode. To list a few, doped $LaCoO_3$ [24], [25], solid solutions of doped $LaMnO_3$ with $LaCoO_3$ and $LaCrO_3$ [26], $Sm_{1-x}Sr_xCoO_3$ [27], [28], $Pb_2Ru_2O_{6.5}$ [29] and $La_{1-x}Sr_xCuO_{2.5-\delta}$ [30] have been experimented as some popular cathode materials.

The most recent focus on the development of SOFC research is to reduce the operating temperature from high to the intermediate range (500-800 °C). At intermediate temperature, the number of choices for electrode materials increases, which favors the cell

manufacturing cost. The formation of insulating zirconate layer due to the reactions between the electrolyte and electrode that occurs at the higher temperature can be restricted. However, the operating temperature reduction is associated with two key issues. The rate of reduction reactions becomes slow. Moreover, the contact between the cathode and the electrolyte becomes poorer as the sinterability is reduced, deteriorating the cell performance.

MIECs such as $La_{1-x}Sr_xCo_yFe_{1-y}O_{3-\delta}$ (LSCF), $Sm_{0.5}Sr_{0.5}CoO_{3-\delta}$, and $Ba_xSr_{1-x}Co_yFe_{1-y}O_{3-\delta}$ (BSCF) have been extensively investigated as IT-SOFC cathode [27], [28], [31], [32], [33] The use of MIECs as cathodes increases the rate of oxygen reduction at the electrolyte-electrode interface as TPB extends over the electrode surface. Among these materials, $La_{1-x}Sr_xCo_yFe_{1-y}O_{3-\delta}$ (LSCF) showed a matching CTE with the oxide electrolyte material, high electrical conductivity and good ORR catalytic activity [34], [35].

The literature on $La_{1-x}Sr_xFeO_{3-\delta}$ (x=0.0-1.0) perovskites (LSF) as a cathode material for SOFC indicated that Sr-substitution at La-site alters the oxygen stoichiometry and consequently, the electrical and electrochemical behavior. The data on the electrical and electrochemical behavior of LSF showed quite scattering as per the Sr-substitution level at A-site is a concern [36], [37]. $La_{1-x}Sr_xCo_{1-y}Fe_yO_{3-\delta}$ perovskites with Co- compositions, particularly $La_{1-x}Sr_xCo_{0.8}Fe_{0.2}O_{3-\delta}$ exhibits improved electrical, electrochemical behavior [38]. However, Co-rich perovskites possess high CTE and prone to deleterious reactions with Zr based electrolytes [39]. Fe-rich composition especially $La_{1-x}Sr_xFe_{0.8}Co_{0.2}O_{3-\delta}$ has showed good thermochemical stability with the SOFC electrolyte [40], [41], [42]. Nanostructured electrode powder is used to avoid the disadvantageous reaction between the electrode and the electrolyte as they can be sintered at a low temperature.

Moreover, the application of nanostructured cathode material also increases the effective TPBs for electrochemical reactions [43], [44]. The powder preparation method has a significant effect on the microstructure, particle size distribution, and surface area of the resulting particle [32], [45]. Morphology of the electrode powder also affects the performance of the electrode.

1-2-5 Anode

The focus of this study is primarily cathode and interface nano optimization, with some focus on electrolytic materials as well. However, the final component of SOFCs is the anode, a detailed investigation of which is outside the context of this study. Many of the requirements of the SOFC anode are like those of the cathode. The anode material must exhibit high catalytic activity for the hydrogen oxidation reaction, should have excellent electronic conductivity for electron transport from TPB sites to the external circuit, and should show at least marginal ionic conductivity to maximize the TPB site density. The anode material should have sufficient chemical and mechanical stability to withstand the high-temperature oxidation environment of the anode and the repeated reduction/oxidation (redox) cycles required for regular operation. The material should be chemically compatible with other SOFC components such as the electrolyte, and the circuit interconnects materials. It should also have a thermal expansion coefficient that matches relatively well with other SOFC components. The anode should be sufficiently porous (>30 vol%) to allow permeability of gaseous fuel, and should sufficiently stable to maintain performance after the extended operation (>90,000 h).[9]

The most widely used SOFC anode material is a Ni-YSZ composite “cermet” material (material that is comprised of both a ceramic and a metal component). In Ni-YSZ anodes, nickel provides the high catalytic activity and electronic conductivity, and the YSZ provides the ionic conductivity, structural support, aids in the matching of thermal expansion between the anode and electrolyte and suppresses agglomeration of nickel particles during operation which is a widespread problem for pure Ni anodes. Ni-YSZ anodes are incredibly stable in high-temperature oxidation environments, and they virtually satisfy all the requirements for a SOFC anode. As with the cathode, a multi-layer approach is often used to improve performance and maximize thermal expansion compatibility.[8]

1-3 Atomic layer deposition

Atomic layer deposition (ALD) is a vapor phase growth technique mostly used to deposit thin films. This method is strong due to its unique process of growth. Typically, two or more highly reactive precursors are pulsed into a reaction chamber sequentially. Each pulse of precursors followed by a pulse of oxidant material to make a metal oxide layer. They react separately, irreversibly, and in a self-limiting manner at the surface without decomposition. The thickness of the film is controlled at the angstrom level by the number of ALD cycles applied.

ALD is a cyclic version of the chemical vapor deposition (CVD) method. Instead of fluxing the chemicals continuously into the reaction chamber, ALD breaks down the deposition process into two or more segments by keeping the reaction chemicals separate during the process. In a typical ALD process, one of two chemicals is a metal precursor, and the other is the oxidant. The substrate, or the surface on which the film needs to grow, is exposed to these two chemicals one at a time in a cyclical manner. This way, the thin film is deposited and grown onto the substrate in a precisely controlled fashion.

ALD was developed in the 1970s by T. Suntola and coworkers to meet the needs of the industry for dense and pinhole-free films in thin-film electroluminescent (TFEL) displays. ALD was used in the production already in the early 1980s, but the big breakthrough for the ALD technology came at the beginning of the 21st century. The continuous down-scaling of microelectronic devices was the reason for the growing interest in ALD. The first microelectronic application was in dynamic random-access memory (DRAM) capacitors, where ALD of Al_2O_3 was used as an insulating layer. One of the largest publicities around ALD came when Intel announced that ALD of HfO_2 would be used in the manufacturing of complementary metal-oxide-semiconductor (CMOS) transistors.[47] The diagram in Fig.1-6 shows the number of ALD publications per year from 1980 to 2016, revealing increasing interests for ALD in many areas of nanotechnology research.[48]

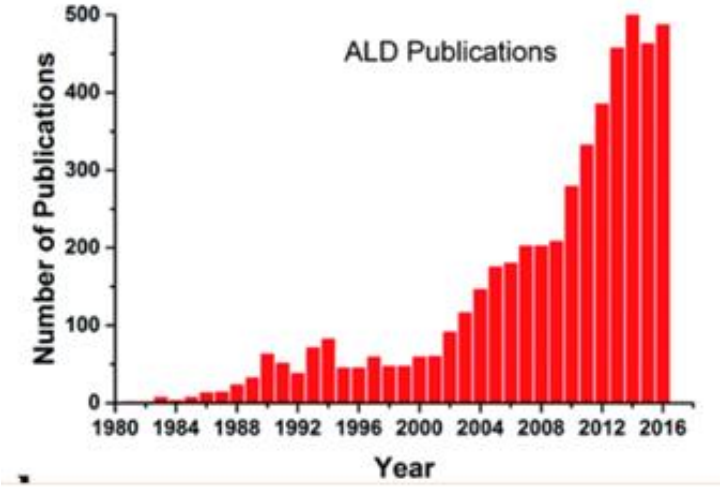

Fig. 1-6 The number of scientific publications on ALD published per year from 1980 to 2016 based on information.[52]

The precursor used during the ALD proces is a chemical compound, which is composed of a metal atom surrounded by ligands. The metal atom is the element to be deposited; ligands generally serve the protective role of the "naked" atom and can only be oxidized and removed through reacting with the substrate or the oxidant.

A variety of oxidants can be used in the ALD process. Based on the oxidation strength required in the reaction, certain oxidants are needed to deposit a specific material. Common oxidants are distilled water, hydrogen peroxide, air, oxygen, oxygen plasma, and ozone. An example of the reactions occurring during one ALD cycle is illustrated in Fig.1-7. The ALD cycle starts with the pulsing of precursor 1 (Fig.1-7a) typically a metal reactant, followed by gas-solid reactions (chemisorption) onto the substrate (Fig.1-7b). When the surface is saturated with the first precursor, inert gas purges (Fig.1-7d) the redundant precursors and by-products as have shown in Fig.1-7c. The second precursor is introduced (Fig.1-7e), which is typically a non-metal reactant, to react with the ligands of precursor 1 (Fig.1-7f). Again, unused precursors and by-products are removed by inert gas purging (Fig.1-7g). By repeating steps a-g, the ALD film grows in a layer-by-layer fashion (Fig.1-7h). The thickness after one ALD cycle is ideally one monolayer, but in practice, it

is less due to steric effects. These reactions follow an exchange-type growth mechanism. ALD of Al_2O_3, which is an ALD model system, follows this reaction scheme.[49]

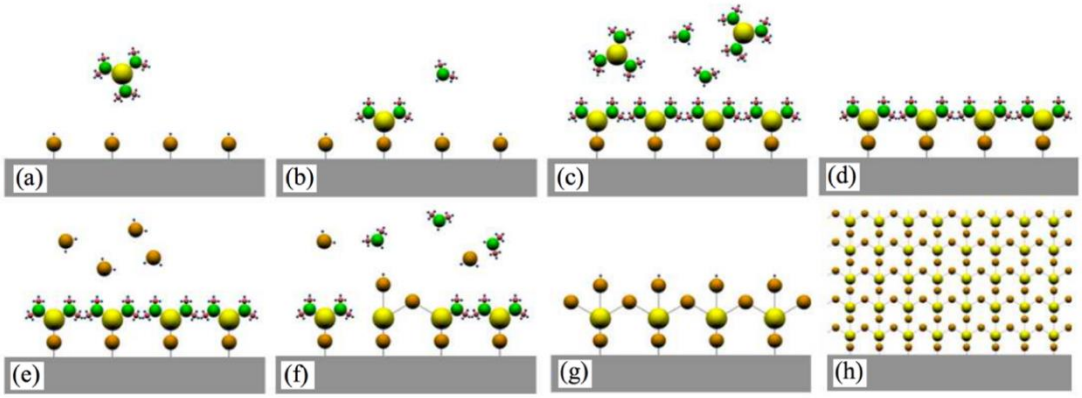

Fig. 1-7 Illustration of one ALD reaction cycle. (a) The pulse of precursor 1. (b) Reaction at the sample surface. (c) The reaction is self-limiting. (d) An inert gas purges excess precursors and by-products. (e) A pulse of precursor 2, e.g., O_2 or H_2O. (f) The reaction at the sample surface. (g) Inert gas purging of excess precursors and by-products. (h) By repeating steps (a)-(g), the ALD film grows layer by layer. Schematic adapted from [46].

There are different growth modes for ALD, illustrated in Fig.1-8. Where the growth rate is plotted as a function of deposition temperature. The ALD window is the deposition temperature range, where the growth rate is constant. When the growth temperature is too low, precursor condensation or low reactivity of the precursors will occur. At temperatures above the ALD window, precursor decomposition or precursor desorption might be observed.

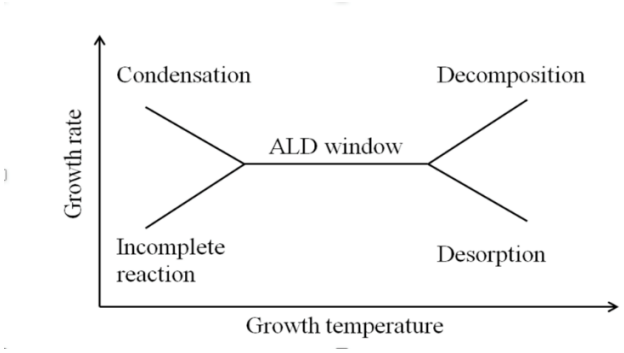

Fig. 1-8 Illustration of the ALD window, where growth rate is independent of the temperature [50].

Generally, as a result of the self-limiting characteristic, ALD films are conformal, even on high aspect-ratio structures.[50] This is the main feature that distinguishes ALD from other thin film deposition methods. ALD films are typically also of high quality, e.g., pinhole-free, due to the layer-by-layer growth mechanism. In many cases, ALD processes have a relatively low growth temperature with a full temperature window as the reactions do not rely on a decomposition of precursors (like in chemical vapor deposition). High uniformity over large areas, good reproducibility, low vacuum requirements and lack of sensitivity to excess precursors also make ALD suitable for batch production. Due to the digital nature of film growth, i.e., thickness controlled by several ALD cycles, creating multilayers, mixed, graded, or doped layers are also easily achievable, making ALD a flexible deposition technique.[51], [52]

One of the most severe limitations of ALD has been the low deposition rate, which is a problem when thick films need to be grown. However, with the downscaling of microelectronic devices and the gradual maturity of thin-film applications in nanotechnology research, the time tạken to deposit weak layers has become quite practical. With the recent advances in high-speed spatial ALD, even thick films are now obtainable with reasonable processing time. [53]

Another major drawback in ALD is the limited choices of available processes for materials (mostly oxides). In recent decades, several researchers have been developing new precursors and processes to fill the gaps. There is now a good number of ALD processes for metals, nitrides, and chalcogenide material systems to choose from.[54]

In this research, ALD is a suitable thin film deposition process to grow YDC, YSZ, and other metal oxide coatings and interlayers. In the ALD process, there are several critical parameters in determining the quality and property of the resulted thin films.

1. Reaction temperature: This is also the substrate temperature in the ALD deposition. Thin film’s growth per cycle is a function of the reaction temperature, and only within a specific temperature range, will adsorption-limited saturating deposition

occur. We call this temperature range the ALD window. To precisely control the film thickness, we need first to identify the ALD window of the deposited material. Varied materials have different ALD windows. For a multicomponent material, such as YDC, the reaction should be carried out within an overlapped temperature range governed by ALD windows of the respective metal precursors.

2. Precursor temperature: The precursor needs to be heated above its sublimation temperature to generate gaseous chemicals. However, this temperature cannot be set too high to avoid vibrant vapor flow. Sometimes, precursors can decompose under elevated temperatures, which leads to carbon contamination in the deposited films.
3. Pulse time: There is also an optimal pulse time for each precursor or oxidant. Due to the self-limiting feature of ALD, sufficient chemicals need to be provided in order to reach full reactions. However, providing more than needed chemicals will result in a waste of time and material.
4. Purge time: After each deposition, excessive chemicals (either oxidants or precursors) and reaction products should be thoroughly purged out of the chamber. Otherwise, they will interfere with the following deposition cycles and create impurities in the resulting films. Thus, we need to maintain enough purge time to clean the chamber. However, the ALD process is already a slow film growth technique, and purging usually takes up the majority of the whole deposition time. Therefore, we determine the minimal time needed to purge the chamber.
5. Precursor/oxidant selection: At times, there is more than one candidate that can be employed as the precursor or oxidant chemicals. The above four parameters could be different depending on the chosen chemical. Therefore, precursor and oxidant selection is also part of the entire process of determining the optimal deposition conditions of ALD

1-4 Electrochemical characterization methods

Several methods exist for characterizing the performance of SOFCs, including, but not limited to: electrochemical impedance spectroscopy (EIS), current-voltage (I-V) characterization, and open-circuit voltage (OCV) measurements. In the present study, experiments are conducted using either symmetric cells (which has two cathode electrodes) or full cell (which has one cathode and one anode) with a significant focus on the cathodic reactions. Current-voltage characterization and open circuit voltage measurements are generally only used for full cell characterization. Electrochemical impedance spectroscopy is the primary characterization methods used in this study.

1-4-1 EIS characterization

There are two operating modes in EIS, called potentiostatic and galvanostatic. In potentiostatic mode, a low-amplitude, alternating potential is applied to the electrochemical cell, and the current response is measured. For galvanostatic mode, a current perturbation is made to the cell while the potential is monitored [55]. By applying a small excitation signal, the response is pseudo-linear and expressed by a magnitude and a phase shift. The impedance Z can be calculated and plotted in a Nyquist plot, with the real part of the impedance on the x-axis and its imaginary part on the y-axis. An example is shown in Fig. 1-9a. Each point on the complex plane plot is the impedance at one frequency ω.

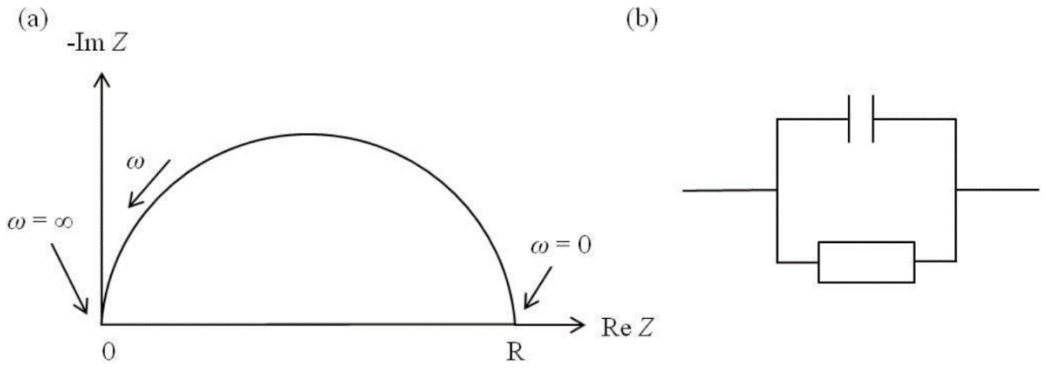

Fig. 1-9 (a) Example of a Nyquist plot and (b) its equivalent electrical circuit.

EIS data are commonly analyzed by fitting it to an equivalent electrical circuit model as each physical process in the electrochemical cell, e.g., electrolyte resistance and polarization resistance has characteristic impedance behavior and can be considered as an electric component or a simple electrical circuit. The model can be a combination of resistances, capacitances, and/or inductances, as well as a few specialized electrochemical elements such as Warburg diffusion elements and constant phase elements. It produces the same response as the electrochemical system does when the excitation signal is applied. A resistor and capacitor described in the equivalent circuit (Fig.1-9b) is used to fit data to a Nyquist plot in Fig. 1-9a.

In order to develop a complete test of SOFC single cells and to refine their efficiency and long-term stability, the performance-related polarization processes have to be identified and proven. In contrast to I-V curves, where only the overall loss of a cell can be identified, the EIS is one of the most promising methods for unfolding complex electrochemical processes in a cell.

The EIS method takes advantage of the fact that the polarization loss mechanisms taking place in an electrochemical system differ in their characteristic time constant and frequency response. The most common and standard approach to measure the dynamic behavior (impedance) of an electrochemical system is by applying a sinusoidal current (or voltage) to the interface and measure the phase shift and amplitude, or real and imaginary parts, of the resulting voltage or (current). Here it should be noted that impedance is only defined for systems that satisfy the conditions of causality, linearity, and time-invariance. Although many systems, like SOFCs, are usually non-linear, linearity can be assumed when the magnitude of the applied current stimulus is small enough to cause a linear response.

A sinusoidal current of small amplitude $i(t) = i_0 \sin(\omega t)$ is superposed to a defined bias current load and the sinusoidal voltage response $u(t) = u_0(\omega)\sin[(\omega t+\phi(\omega)]$ is measured. From the ratio between the complex variables of voltage and current, the impedance is calculated as follows (Eq. 1-2):

$$Z(\omega Z(\omega) = \frac{u(t)}{i(t)} e^{i\varphi(\omega)} = |Z(\omega)|e^{i\varphi(\omega)} = Re\{Z(\omega)\} + jIm\{Z(\omega)\} \quad \text{Eq.1-2}$$

Where $\omega=2\pi f$ [s^{-1}] represents the angular frequency and $\phi(\omega)$ the frequency dependent phase shift between voltage and current.

This measurement is generally performed for a discrete quantity of frequency values in a defined frequency range, and the recorded impedance values are usually plotted in the complex plane. The resulting curve is also known as the Nyquist plot. Fig.1-10 gives an example for a Nyquist plot measured on a SOFC single cell. The high frequency intercept with the real axis corresponds to the purely ohmic resistance R_0 of the cell, whereas the intercept at the lower frequency is identical to the differential resistance, which can be obtained from the corresponding I-V characteristic at the given operating point. The difference between the low and high frequency intercept is the so-called polarization resistance R_p of the cell. R_p is the sum of each single polarization resistance caused by the loss mechanisms.

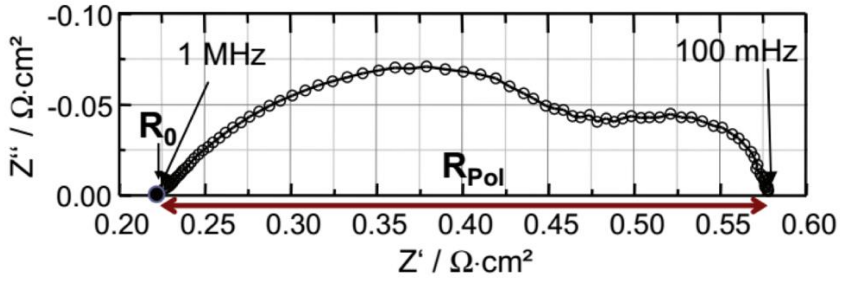

Fig. 1-10 Typical Nyquist-plot recorded on a SOFC single cell. The high frequency intercept with the real axis corresponds to the purely ohmic resistance R_0. The difference between the low and high frequency intercept is the so-called polarization resistance R_p of the cell.

Chapter 2 Literature review: Nanoscale treatment on SOFC electrode and interface materials

There are several ways to improve the SOFC materials at the nanoscale. Nanotechnology offers vast opportunities for applications in the SOFC field and the development of electrode, electrolyte and interface materials. Advanced materials engineering based on nanoscience have led major breakthroughs in fuel cell systems. In this chapter, some of the applications of nano treatments are discussed. Then, three approaches of nanoscale surface and interface treatments that were applied to my study are introduced. Here we gathered a list of nanoscale applications that have significant impacts on the improvement of SOFCs. The main applications for electrolyte and interlayer nanotreatments are:[56]

1- To increase oxide ion conductivity up to a commercially viable level (~0.1 S/cm at operating temperature) by nanoscale treatments . In addition, ohmic resistance can decrease using thin dense nano-coating methods.
2- To keep electronic transference number very low ($<10^{-3}$) for electrolyte by applying nanocoatings to prevent pinholes, in thin electrolytes. This has not been readily achievable without the help of nanoscale coating techniques.
3- To enhance thermodynamic and chemical stability over a wide range of temperatures (from room temperature to 1000 °C) at variable activities of oxygen ($1–10^{-22}$ atm). Surface decoration and also controlling the ratio of materials on the atomic scale can improve the chemical and thermodynamic stability of the material.
4- To provide chemical inertness for electrode materials during both processing and service. To prevent the electrode-electrolyte interaction, a thin layer of an inert interface can be applied between them by the use of nano deposition.

Nano treatments can also help cathode to possess the following functionalities for the efficient operation of SOFC:[56]

1- Increasing electronic conductivity (> 100 S/cm in an oxidizing atmosphere) by adding nanomaterials during the fabrication process.
2- Minimizing the mismatch between the coefficient of thermal expansion (CTE) values of the cathode and other components of the cell, such as electrolyte and interconnect materials.
3- Enhancing chemical compatibility with the electrolyte and interconnect materials
4- Grow porosity to allow fast diffusion of O^2 gas from cathode to cathode-electrolyte interface.
5- Boosting oxide ion conductivity inside electrode materials.
6- Increasing stability under an oxidizing atmosphere during fabrication as well as operation;
7- Enhancing the catalytic activity of electrodes during ORR by tailoring the TPB lengths and increasing the area of active reaction sites. Also, by increasing surface energy with thin oxide coating on electrode materials.
8- Making it more cost-effective in terms of fabrication by using nanomaterials that replace or reduce used amount of precious metals.
9- A nanoscale surface decoration that helps precisely mix oxides or decorate the surface by our desired materials.
10- Increase the durability of cathodes by applying a few tens of microns of metal oxides on the electrode surface.
11- Lowering working and fabrication temperature of SOFCs.

There are different methods for nanoscale treatments. Among them, we have used three techniques that are considered to have high impacts on SOFC performance. In the next parts of this chapter, they are introduced, and the state-of-the-art methods on each category have been presented. The first one is the effect of sintering aid on improving the mechanical and electrochemical behavior of SOFC electrode and electrolytes. There are many reports which studied the impact of different sintering aid materials (notably cobalt oxide). Researchers have shown it helps grain growth and interconnectivity and allows lowering the sintering temperature of SOFC materials. However, there have not been explicit studies

about the optimization of sintering aid for LSCF and LSCF-GDC composite cathode materials. Thus, In the first study, we focused on the effect of cobalt oxide as a sintering aid on these cathode materials in terms of microstructure and cathodic performance.

2-1 ALD treatments

As briefly explained in the introduction part, ALD is based on successive, surface-controlled reactions of gas phase precursors with a substrate to produce a thin coating with excellent conformality and process controllability.[77] ALD enables to render uniform, homogeneous, and dense thin films even on highly corrugated surfaces by building a mono-atomic layer after another. Atomic level control ensures that atomic-scale films, even on complex nanostructures, can be formed.[78] ALD can also be used to modify the interfaces or dope a film at the desired level, even the level of delta-doping.[78]

The first SOFC material processed by ALD was YSZ, which was grown from cyclopentadienyl- or chloride-type precursors together with ozone or water as the oxygen source.[4],[5] This ALD process was based on the earlier ones developed already in the 1990s for its constituents, viz. Y_2O_3 and ZrO_2.[81],[82] Besides, Shim et al.[83] have likewise combined the individual organometallic yttria and zirconia processes to obtain freestanding 60 nm films with Pt electrodes on both sides of the YSZ electrolyte. The observed high-power density of 270 $mWcm^{-2}$ at 350 °C was attributed to low electrolyte resistance and active electrode kinetics. Also, the nanoporous structure of Pt electrode and nanocrystallinity of YSZ was conjectured to be beneficial factors.[84] From these examples, ALD has been a powerful tool to realize high performance small scale SOFCs.

ALD has been successfully used to deposit SOFC electrodes. Several sources cite the use of ALD to deposit thin film Pt layers to be used as highly catalytic SOFC electrodes.[95]–[97] Holme et al.[98] successfully deposited LSM cathodes using ALD for micro LT-SOFCs. For the deposition of an MIEC cathode such as $La_xSr_{1-x}MnO_3$ (LSM), the ALD cycle becomes complicated as the feeding of three different precursors and an oxygen source are to be synchronized in a chamber.

Furthermore, the oxides of La and Sr are known to readily react with the carbonate impurities originating from the precursors and present in the reactor.[99] Nevertheless, using Cp-type organometallic precursors together with water, Holme et al.[100] developed a satisfactory ALD-process where LSM was crystalline as deposited on YSZ and further annealing treatment did not change the morphology and crystallinity of the layers significantly. These authors found that, unfortunately, the LSM fabricated cathode was not of sufficient quality for low-temperature operation. A low peak power density of 0.2 μWcm^{-2} was achieved at 450 °C with LSM deposited on YSZ with a Pt anode.

Another cathode material that was deposited by ALD is $La_{1-x}Ca_xMnO_3$. ALD can deposit it at 200 – 330 °C, using $La(thd)_3$, $Ca(thd)_2$ and $Mn(thd)_3$ organometallic precursors together with O_3 as oxygen source, as recently demonstrated by Nilsen et al.[101] Even though the field of ALD processed SOFC cathode materials has not been widely investigated, the aforementioned studies show the feasibility of growing multicomponent phases with well-controlled cation stoichiometry.

Several studies have shown that surface processes such as adsorption of molecular oxygen onto surface vacancy sites are the most probable rate-limiting step for perovskite cathode materials such as LSCF and that these processes can be improved by using various surface modification techniques.[102]–[106] In addition to electrolyte and electrode deposition, ALD has also been used more recently to modify existing electrodes to improve performance and durability. Gong et al.[107] investigated the use of ALD to improve the durability of $La_{1-x}Sr_xCoO_3$ (LSCo)- $La_{1-x}Sr_xGa_{1-y}Mg_yO_{3-0.5(x+y)}$ (LSGM) composite cathodes. It was shown that the cathode exhibited excellent durability over 4000 h of operation by depositing a thin layer of ZrO_2 via ALD, with the polarization resistance increasing about 18 times more slowly than the untreated sample. The authors conclude that the addition of a ZrO_2 overcoat suppressed particle agglomeration and surface Sr-segregation, both of which are significant causes of cell degradation. Although ZrO_2 deposition by ALD improved performance for LSCo cathodes, Rahmanipour et al.[108]

found that ZrO_2 deposition blocked active reaction sites for LSF cathodes, dramatically hindering performance.

Yu et al.[109] evaluated the effect of CeO_x deposition by ALD on the performance of LSF, LSCo, and BSCF cathodes. It was shown that ceria particles preferentially reacted with oxygen vacancies on the surface of the LSF cathode, impeding oxygen adsorption, and thus significantly increasing the electrode impedance. This conclusion was confirmed by ceria deposition on BSCF and LSCo cathodes; BSCF has a much higher concentration of oxygen vacancies at the surface, and LSCo oxygen vacancies are comparable to that of LSF. Consequently, BSCF was much more tolerant of ceria deposition, showing a lesser decrease in performance, and LSCo showed a decrease in performance that was similar to LSF.

Gong et al.[110] further investigated the ALD deposition of ZrO_2 onto LSCF-GDC composite cathodes. The authors found that the ALD treatment lowered the cathode polarization resistance by 3 times, lowered the ohmic resistance by 1.5 times, and improved long-term durability by 4 times. They concluded that this was due to increased porosity, increased ionic conductivity, and suppressed surface Sr-enrichment by the ZrO_2 overcoat. Sholklapper et al.[111] showed that LSCF cathodes infiltrated with YDC dramatically increased the ionic conductivity of the electrode, causing a decrease in ohmic resistance for the infiltrated electrode as compared with a bare LSCF electrode.

2-2 Nano treatment of cathode-electrolyte interfaces

For IT/LT- SOFCs, activation polarization, especially on the cathode, are significantly more pronounced under these conditions than normal HT-SOFCs. This is primarily attributed to the sluggish kinetics associated with the decreased temperature operation.[112] It was found that the electrocatalytic activity or electrode/electrolyte interfacial characteristics were enhanced through the addition of the thin nano interlayers.

This performance improvement was attributed to the introduction of a diffuse mixed conduction region associated with these interlayers. These thin film composite interlayers improve charge transfer reaction in the electrode/electrolyte interface for both anode and cathode sides. The nature of these interlayers is still a matter of contention, and further studies are required to understand their function adequately. The objective of a vast number of efforts was to characterize the anode and cathode performance enhancement of thin film SOFCs when anode and cathode interlayers are included between the electrode and electrolyte interface. This interlayer surface can also be achieved by using ALD between electrode-electrolyte.

The ohmic loss through electrolytes is a major cause of power loss, severely limiting SOFC performance. The ohmic resistance of a SOFC is highly dependent upon electrolyte thickness, and thus, much research has been conducted to minimize electrolyte thickness. Several studies have shown that thin film electrolytes of YSZ and GDC deposited by ALD significantly improve performance as compared with conventionally deposited electrolytes.[85]–[88] Additionally, ALD has been used to modify the surface of SOFC electrolytes to improve performance. Fan et al.[89] showed that the cathode/electrolyte interfacial resistance could be dramatically decreased by depositing an ultra-thin layer of YDC between the YSZ electrolyte and Pt cathode.

Ceria-based ceramic electrolytes have an ionic conductivity superior to that of zirconia-based electrolytes.[90] There are a vast number of applications of ceria-based electrolytes, either as a double-layered electrolyte (mostly with zirconia-based one) or as a single layer electrolyte for LT-SOFCs. Therefore, ceria-based oxides such as GDC, being widely used in SOFC devices, are good candidates for future technology. As the ALD processes for depositing gadolinia and ceria are well-established,[91], [92] the only primary engineering task for depositing doped ceria is to find a proper ratio of ALD cycles for gadolinia and ceria and address the differences in optimum temperature of ALD. Experiments performed by Gourba et al.[93] have focused on making GDC by using the correct corresponding precursors' ratio. They prepared GDC with $Ce(thd)_4$, $Gd(thd)_3$, and

ozone precursors on Si, LSM, and Ni-YSZ substrates. High quality and dense layers were obtained on both planar and porous substrates. However, there was a challenge due to unstable stoichiometry control and a low growth rate (0.4 Å/cycle). Considering that Y^{3+} has an ionic radius similar to that of Gd^{3+} and that ALD processes for Y_2O_3 are well-established,[80] Ballée et al.[94] processed YDC by ALD at 300 °C also using the (thd) precursors and ozone. Conformal, dense and crystalline as-deposited YDC films were obtained with an excellent stoichiometry control. At temperatures higher than 420 °C, the conductivity of YDC becomes higher than that of YSZ thin films deposited under similar conditions.

Chapter 3 Impact of ALD on oxygen reduction catalysis of porous platinum

In SOFCs, we observe that the porous electrodes tend to agglomerate and thus decrease the cell performance over time. The agglomeration (or sintering) of a porous oxide can be understood as the diffusion of the oxide atoms along the surface of a material to minimize the surface energy of the structure. Therefore, even an ultrathin overcoat is expected to deter the sintering process and thus maintain the porous geometry for longer period of time. In this section, the actual role of YSZ overcoat in the ORR process is presented through a series of electrochemical analyses. Without an overcoat, a nanoporous Pt is significantly agglomerated during a high-temperature operation, and ORR kinetics becomes limited by the availability of TPB. An ultrathin YSZ overcoat significantly suppressed the sintering kinetics and preserved the morphology of its underlying Pt layer. More importantly, the overcoat acts as an excellent facilitator of the atomic oxygen species-mediated chemical process(es), which used to be rate-limiting in the ORR of a non-coated Pt/YSZ system.

3-1 Background of oxide coating on Pt electrode and our approach

Recently, increasingly more studies have been performed on SOFCs because of its advantages in terms of fuel flexibility, system simplicity and efficiency.[2], [113] However, one of the major drawbacks in SOFCs is limited lifetime when operated at high operating temperatures (above 800 °C).[10], [114], [115] While intense efforts are being made to reduce the operating temperature down to the intermediate (600 – 800 °C) or low (< 600 °C) temperature region. The approach, however, results in a significant loss of kinetics in both ionic transport and electrode reaction.[116]–[120]

At low temperatures, the main voltage loss occurs at the cathode. Porous Pt is regarded as the most active ORR catalyst especially at low temperatures although it is expensive and rare.[121]–[123] To achieve higher ORR kinetics, the surface area of the cathode should be maximized, and thus the particle-like features forming the porous cathode should be small. However, these small particles tend to agglomerate fast during operation. This agglomeration will result in a significant decrease in catalytic activity increasing the polarization resistance of the cathode. One of the best-proven techniques to prevent agglomeration of small particles is interfacing them with an oxide[124]–[131] by CVD and wet chemistry.[132], [133]

Among many techniques, ALD is the most ideal tool to achieve a uniform and atomically thin oxide coating on a highly corrugated and porous electrode structure. The self-limiting nature of ALD enables the accrate control of stoichiometry and reproducibility of atomic scale overcoats.[134]

In our recent study, an ultrathin layer of YSZ was coated on a highly porous Pt cathode by ALD to suppress Pt agglomeration for an LT-SOFC[135]. Even a few nm thick coating was indeed found to suppress the morphological degradation of the nanoporous Pt significantly, and this was confirmed by other researchers as well [136], [137]. To our surprise, it was also found that the oxide coating significantly enhances the catalytic activity toward ORR even if the oxide is expected to cover (and thus deactivate) part of catalytically active Pt surface area. In this section, a mechanistic study is presented to understand the impact of ultrathin ALD coating on catalytic kinetics, especially of ORR on a Pt/YSZ system.

3-2 Experimental and cell fabrication

Electrolyte supported Pt/YSZ/Pt cells were fabricated for electrochemical characterization. Pt layers of ~100 nm were deposited on both sides of a ~270 μm thick commercial electrolyte (Fuel Cell Materials, USA) with an AC magnetron sputter at 30W with an Ar pressure of 55 mTorr. The Pt electrodes with the active area of 0.37 cm^2 were patterned using a polyimide tape before the sputter deposition. Ultrathin YSZ overcoat was

prepared in a commercial ALD system (Savannah, Cambridge NanoTech). Tetrakis(dimethylamino)zirconium, $Zr(NMe_2)_4$, Tris(methylcyclopentadienyl)yttrium and $Y(MeCp)_3$ were used as the precursors of Zr and Y, respectively. Ar (99.999%) and distilled water were used as the purging gas and oxidant, respectively. The ratio of cycles between ZrO_2 and Y_2O_3 deposition was 4 to 1 to render 8 mol% YSZ. The canister temperatures for ZrO_2 and Y_2O_3 were 85 °C and 160 °C, and the line temperatures were 180 °C, respectively. The chamber temperature was set at 250°C. The ALD supercycles were performed on the porous cathode for 6 times to make a ~3 nm thick YSZ coating. The microstructures of thin films were characterized by a field-emission SEM (Zeiss GeminiSEM) at the operating voltage of 3 – 5 kV.

Electrochemical characterization was performed in a home-made SOFC test setup. Cells with the active area of $0.37cm^2$ were placed between two current-collecting Pt meshes (Goodfellow Co., USA). The cell was enclosed in a furnace in which the operating temperature is controlled at a set point through a feedback loop. Polarization curves and EIS spectra were obtained by using a potentiostat and impedance analyzer (BioLogic SP-240). The EIS was performed with a 20 mV perturbation and a dc bias ranging from the open circuit potential to η =0.4 V at the frequency of 10 – 106 Hz. During the characterization, 50sccm of dry H_2 (99.999%) was fed to the anode while a various combination of O_2 and N_2 (total of 50 sccm) was fed to the cathode side to control the O_2 partial pressure ranging from 0.04 to 1.0 atm. The resulting EIS spectra were fitted to the equivalent circuit using commercial software (EC-Lab®, Bio-Logic Science Instruments).

3-3 Results and discussion

3-3-1 ALD effect on preventing agglomeration and increase performance

Fig. 3-1 shows schematic diagrams of the two various kinds of cells examined in this study. One is a Pt/YSZ/Pt cell in which porous Pt was sputter-deposited on both sides

of a 270 μm thick YSZ substrate. The other cell is based upon the same Pt/YSZ/Pt cell, but an ultrathin YSZ is coated on one of the two Pt layers by ALD (see Experimental Section). We call them BP (bare Pt-based) and CP (coated Pt-based) cells, respectively.

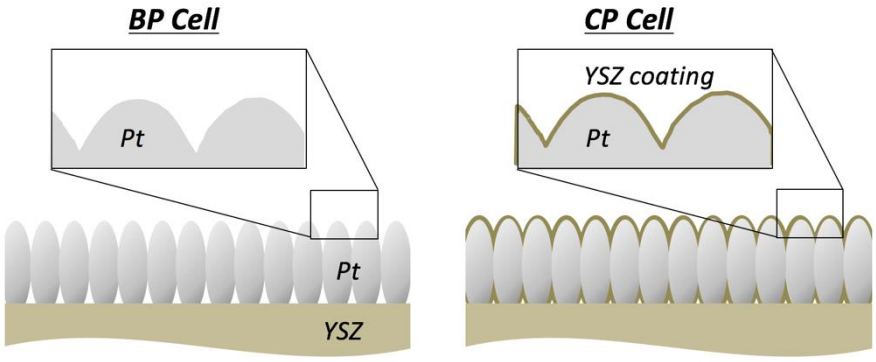

Fig. 3-1 Conceptual drawing of cross-sectional Pt/YSZ with (CP cell) and without (BP cell) the YSZ nano-overcoat

Fig. 3-2 includes time-dependent power densities of the BP and CP cells and corresponding polarization curves obtained after t = 1, 3, and 14 h at 600 °C. Before the measurement, the cells were heated up to 600 °C at the rate of 3 °Cmin^{-1}, and the aging clock started as soon as the temperature of the furnace enclosing the cell reached 600 °C. A continuous cell overpotential η = 0.2 V was applied throughout the aging test except for the duration of intermittent impedance and polarization measurements. The resulting power density with time shows a trend similar to that of our recent study, where a significantly enhanced thermal stability was acquired by applying an ultrathin YSZ overcoat on a Pt-based cathode.[133] The BP cell degraded very fast from the initial power density of 1.57 Wcm^{-2} measured at t = 1 h to 0.26 Wcm^{-2} at t = 14 h under the high-temperature operation. On the other hand, the CP cell maintained its powering capability with a relatively insignificant change from 8.66 Wcm^{-2} to 7.11 Wcm^{-2}. Most of its degradation occurred in the first few hours, and the power density at t = 14 h was 98.7% of the value at t = 5 h.

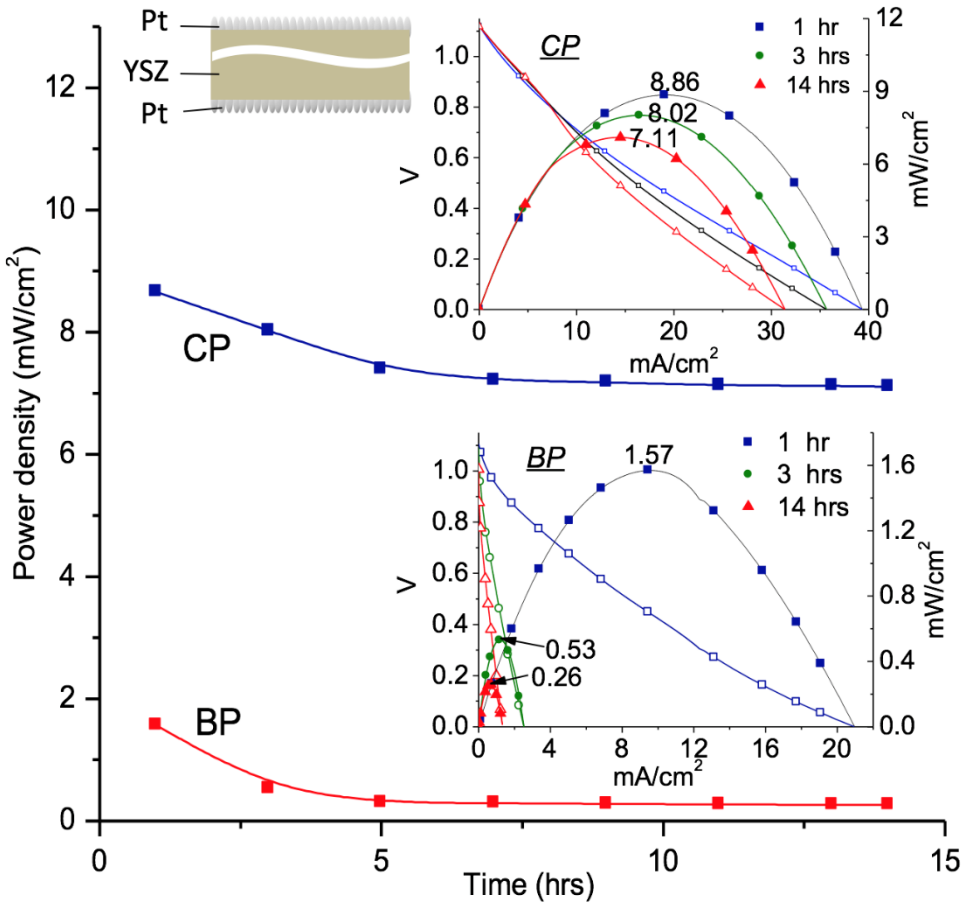

Fig. 3-2 (a) Power density evolution with time under a continuous cell overpotential of 0.2 V at 600 °C. (b, c) Polarization curves and the resulting power density curves of bare Pt/YSZ (BP) and few nanometers YSZ-coated Pt/YSZ (CP) cells. The relatively low power densities are ascribed to the thick YSZ electrolyte (~270 μm) used for this study.

SEM images of cathodes before and after the 14 h-long operations are presented in Fig. 3-3. As reported earlier,[133] an ultrathin ALD-based YSZ coating preserved the nano granular microstructure during the high-temperature operation while the non-coated Pt suffered from a severe agglomeration. Also, the initially uniform YSZ overcoat is conjectured to have agglomerated into nanoscale islands or networks after being exposed to high temperatures,[133] making room for O_2 access to the Pt surface as depicted in the insets of Fig. 3-3.

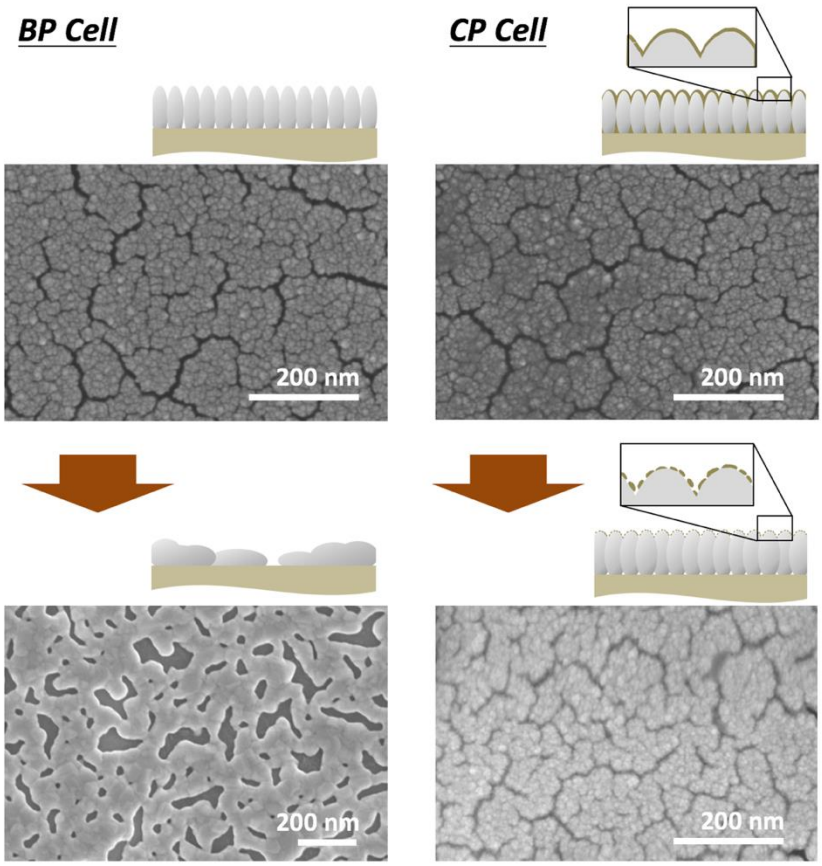

Fig. 3-3 SEM images of the BP and CP cell cathodes before (top) and after (bottom) the 14 h long operation under a cell bias of 0.2 V at 600 °C.

3-3-2 ORR detailed process and ALD impact on R_{ct} components

The ORR process is comprised of its smaller steps. In a Pt/YSZ-based system, these steps are: 1) adsorption of molecular oxygen on the catalyst surface, 2) dissociation of molecular oxygen into atomic species, 3) surface diffusion of atomic oxygen species to the TPB, 4) charge transfer reaction and 5) incorporation of oxygen ions into the electrolyte. In order to better understand the main factors affecting the discrepancy in the performance between the two cells, we first studied ORR kinetics under different oxygen partial pressures (pO_2) ranging from 0.04 to 1.0 atm. The reaction order m, defined in the relation $R_p^{-1} \propto$ slope of $p(O_2)$ (R_p: electrode polarization resistance), provides abundant clues about the rate-limiting step.[136] For example, the reaction order of m =1 indicates that the rate-

determining step is likely related to a molecular oxygen-mediated process such as O_2 adsorption and diffusion. A square root $p(O_2)$ dependence (m = ½) corresponds to an atomic oxygen-related process, including dissociation into atomic oxygen species and their surface transport, and m = ¼ dependence can be ascribed to a process related to the charge transfer reaction.[137]

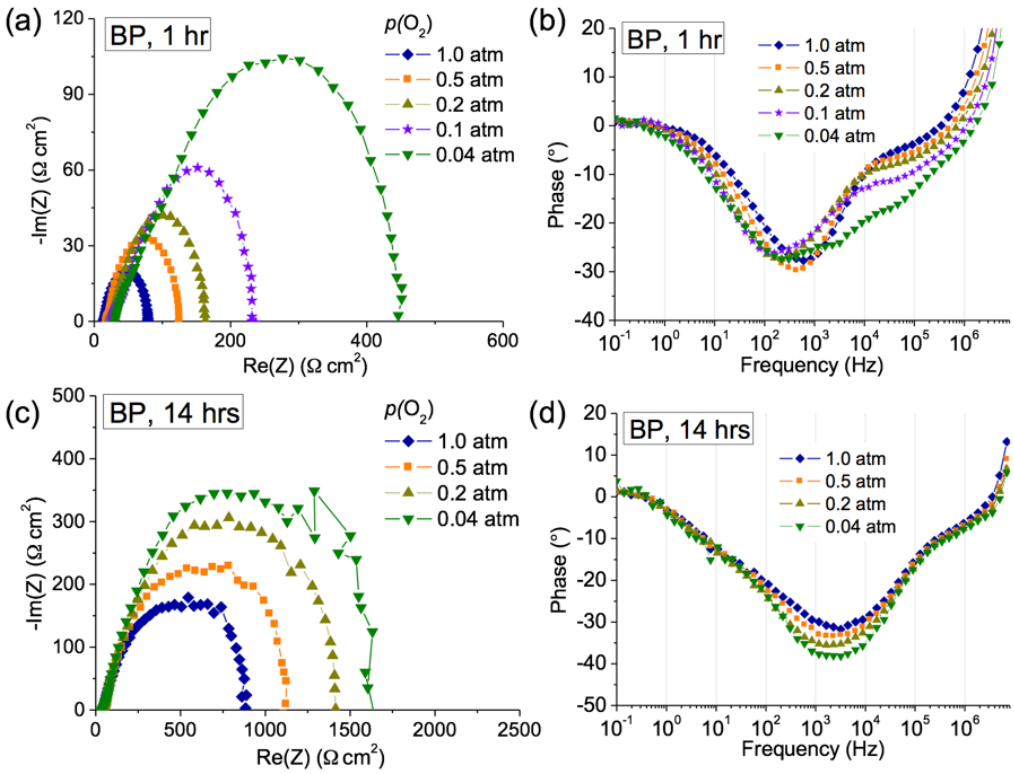

Fig. 3-4 Nyquist (a, c) and Bode plots (b, d) of the BP cell with various $p(O_2)$ at t = 1 and 14 h under η = 0.2 V at 600 °C. Dry H_2 and the O_2/N_2 mixture are being fed to the anode and cathode, respectively. pO_2) is controlled by the ratio of O_2 and N_2 flow rates.

EIS was performed on a BP, and a CP cell and the resulting spectra are presented in Fig. 3-4 and Fig. 3-5, respectively. Each cell was continuously exposed to the operational condition of choice (η = 0.2 V at 600 °C), and a $p(O_2)$ dependency of ORR kinetics was measured at t = 1 h and 14 h. Each EIS was performed only when the electrical current measured at the cell overpotential of 0.2 V had not changed by more than ~3% for 1 min after each $p(O_2)$ change, which usually corresponds to 2 – 7 min.

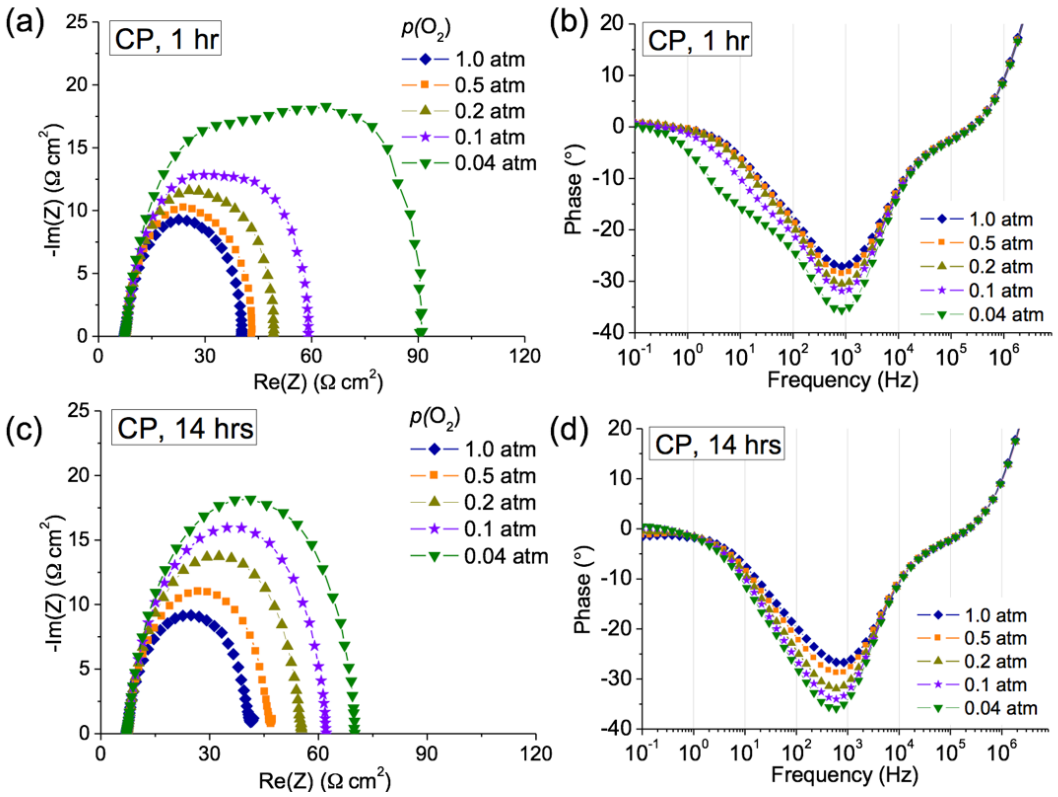

Fig. 3-5 Nyquist (a, c) and Bode plots (b, d) of the CP cell with various $p(O_2)$ at *t* = 1 and 14 h under η = 0.2 V at 600°C.

For both BP and CP cells, the shape of spectra obtained at t = 1 h suggests that at least two R/CPE components can be fitted while it is hard to resolve multiple R/CPE components from those measured at t = 14 h with reasonable accuracy. Therefore, for data fitting, two different equivalent circuits (Fig. 3-5a) were used accordingly to extract each characteristic electrode resistance. The resulting electrode resistances are presented in Fig. 3-5b (BP) and Fig. 3-5c (CP). R_1 is the ohmic resistance originated mainly from ionic transport through the electrolyte, which approximately corresponds to the high-frequency intercept on the real axis of the Nyquist plot. R_2 and R_3 are assigned to the electrode resistances at the higher and lower frequencies, respectively.

It is noted that all the resistance values presented in this report are normalized by the cell area of 0.37 cm^2. The 1 h data fitted to the Equivalent Circuit 1 shows that two distinct electrode processes follow the relation $R_p^{-1} \propto p(O_2)$ slope(m). First, in the BP cell,

the high-frequency resistance (R_2) shows a trend of m = 1.107 (close to 1), which is likely to indicate a molecular oxygen-mediated process.[138], [139] The m value of low-frequency resistance (R_3) is 0.463 (close to 0.5) and is ascribed to an atomic oxygen-mediated process such as dissociation of oxygen into atomic oxygen species and their surface diffusion to the active sites at TPB.[140] R_3 is significantly larger than R2 approximately by order of amplitude throughout the pO_2 range studied here, and the overall ORR process at t = 1 h is thus limited by oxygen dissociation process and/or surface transport of electroactive oxygen species. After 14 h under η = 0.2 V at 600 °C, the overall electrode resistance increased by more than two orders of magnitude, and its pO_2 dependency became m = 0.15, which implies a charge transfer-limited ORR process.[141] Since charge transfer process is known to be much faster than chemically-driven processes such as dissociative adsorption and atomic surface diffusion, the interpretation of m above is well aligned with the fact that the peak frequency at t =14 h are found to be higher than those at t =1 h approximately by an order of magnitude as can be compared in Fig. 3-5b,d.

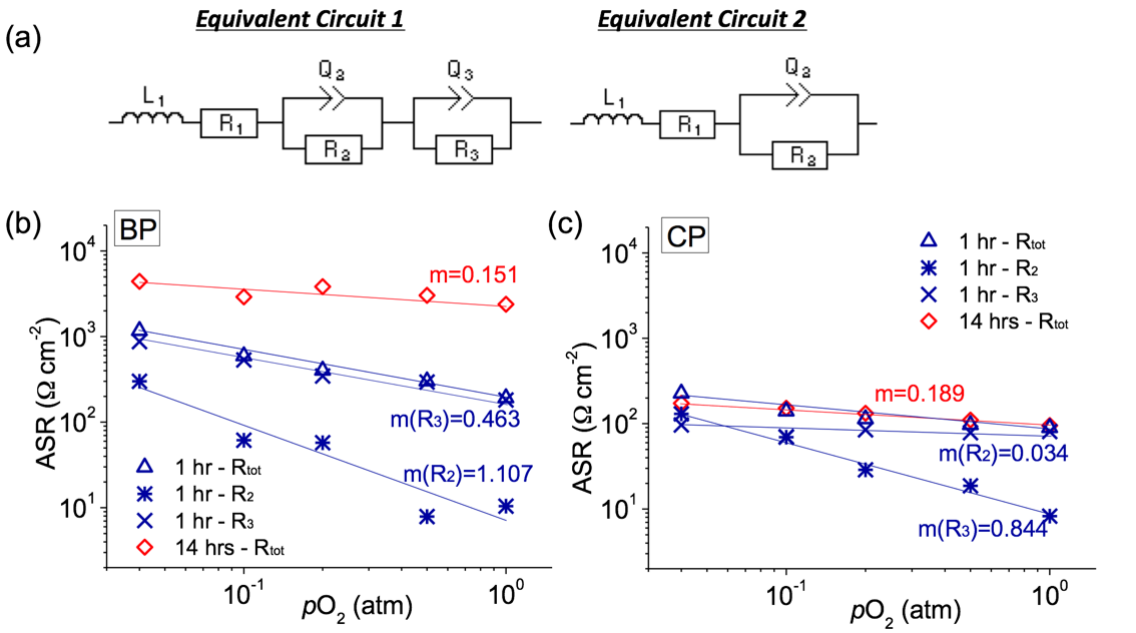

Fig. 3-6 (a) Equivalent circuits used to fit the EIS data. For both the BP and CP cells, equivalent circuits 1 and 2 were used for the data obtained at t = 1 and 14 h, respectively. (b, c) The resulting area-specific electrode polarization resistances of the BP and CP cells as a function of $p(O_2)$. The resulting reaction order, m, was obtained by the least-squares fitting of each dataset.

Table 3-1 Fitted EIS parameters using the equivalent circuits shown in Fig. 6a. Two and one R/CPE components were fitted for the t = 1 h and t = 14 h data, respectively.

		***t* = 1 h**					***t* = 14 h**				
	pO_2 (atm)	0.04	0.1	0.2	0.5	1.0	0.04	0.1	0.2	0.5	1.0
BP	R_1 ($\Omega\,cm^2$)	75.09	58.83	49.86	47.3	27.87	108.5	107.4	118.4	115.5	106.2
	R_2 ($\Omega\,cm^2$)	299.9	61.48	57.61	7.87	10.44	4424	2910	3828	3030	2385
	R_3 ($\Omega\,cm^2$)	874.5	532.4	345.9	293.6	181.4					
	Q_2 ($(Fs)^{1-n}cm^{-2}$)	$6.35\cdot10^{-5}$	$9.81\cdot10^{-6}$	$4.59\cdot10^{-4}$	$1.74\cdot10^{-6}$	$1.05\cdot10^{-6}$	$8.37\cdot10^{-6}$	$2.36\cdot10^{-5}$	$1.02\cdot10^{-5}$	$1.34\cdot10^{-5}$	$1.90\cdot10^{-5}$
	Q_3 ($(Fs)^{1-n}cm^{-2}$)	$2.74\cdot10^{-5}$	$4.10\cdot10^{-5}$	$3.97\cdot10^{-5}$	$3.76\cdot10^{-5}$	$5.15\cdot10^{-5}$					
	n_2	0.452	0.601	0.347	0.843	0.712	0.535	0.479	0.535	0.518	0.50
	n_3	0.679	0.660	0.725	0.70	0.689					
CP	R_1 ($\Omega\,cm^2$)	20.66	20.41	19.89	19.88	18.98	18.65	18.83	18.79	18.78	18.29
	R_2 ($\Omega\,cm^2$)	96.9	70.48	84.7	78.65	81.12	173.8	151.7	132.7	110.1	95.08
	R_3 ($\Omega\,cm^2$)	130.6	69.63	28.86	18.72	8.27					
	Q_2 ($(Fs)^{1-n}cm^{-2}$)	$2.54\cdot10^{-5}$	$2.44\cdot10^{-5}$	$4.05\cdot10^{-5}$	$4.52\cdot10^{-5}$	$5.67\cdot10^{-5}$	$9.01\cdot10^{-5}$	$9.27\cdot10^{-5}$	$1.05\cdot10^{-4}$	$1.30\cdot10^{-4}$	$1.55\cdot10^{-4}$
	Q_3 ($(Fs)^{1-n}cm^{-2}$)	$3.23\cdot10^{-4}$	$2.10\cdot10^{-4}$	$2.16\cdot10^{-4}$	$2.47\cdot10^{-4}$	$2.70\cdot10^{-4}$					
	n_2	0.807	0.815	0.755	0.749	0.729	0.682	0.684	0.673	0.652	0.634
	n_3	0.781	0.828	0.995	1.0	0.999					

This inference is corroborated by dc-bias dependent impedances compiled in Fig. 3-7. The total electrode resistance ($R_2 + R_3$ for 1 h cells and R_2 for 14 h cells) were extracted from impedance data obtained with different cell overpotentials ranging from 0.0 V to 0.4 V. If an ORR rate is limited by a charge transfer reaction, the electrode resistance would follow the Tafel behavior. The ASR for ORR from an impedance measurement is then expressed as:[142]

$$ASR_{ORR} = \frac{d\eta}{dj} = \frac{RT}{\alpha nF}\frac{1}{j} = \frac{RT}{\alpha nF}\frac{1}{j_0}e^{\frac{-\alpha nF}{RT}\eta} \qquad \text{Eq. 3-1}$$

where α: the electron transfer coefficient, n: the number of electrons per species, F: Faraday constant, R: gas constant, T: temperature, j: current density, j_0: exchange current density and η: the overpotential of ORR. According to this equation, the slope from the logarithmic ASR vs. over potential graph can be used to quantify α·n. As for the BP cell at t =1 h, not only the logarithmic ASR vs. η deviates from the linear behavior but also α·n is calculated to be < 0.4, indicating that there is another rate-limiting step other than the charge transfer reaction in this cell. (Note that the usual α is in the vicinity of 0.5) At t =14 h, α·n values become ~0.8, making it reasonable to consider the measured quantities corresponds to the charge transfer process.

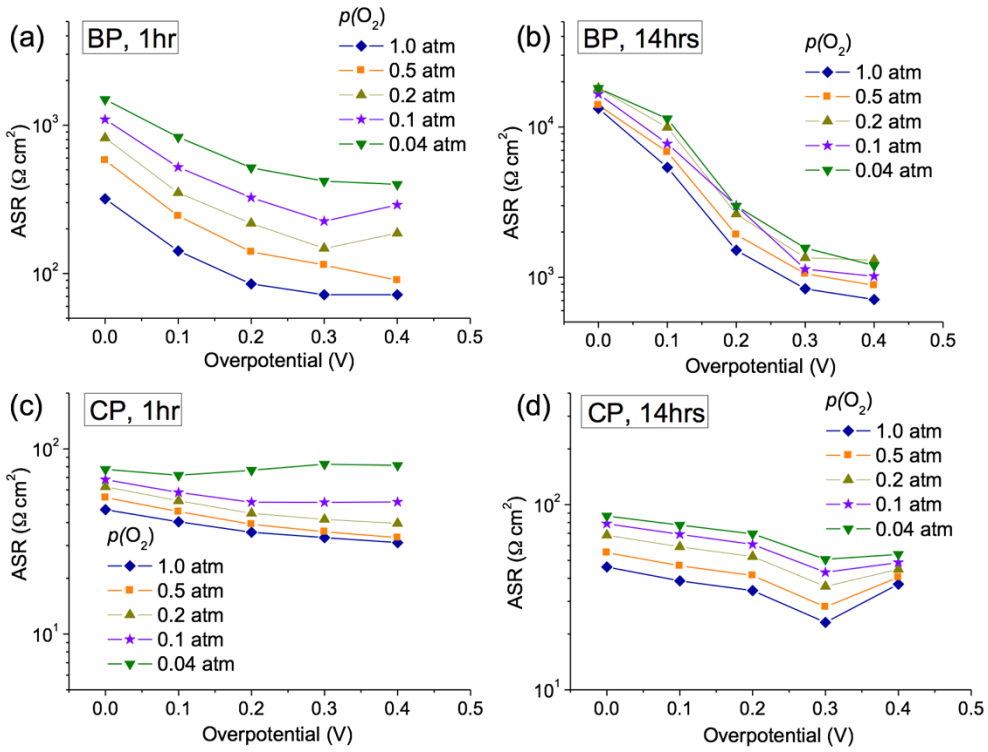

Fig. 3-7 ASRs with cell overpotential η obtained from EIS measurements of the BP and CP cells under various $p(O_2)$. Equivalent circuits are shown in Fig. 3-6a were used to extract the ASRs

On the other hand, the CP cell showed the overall electrode resistances and power densities much smaller than those of the BP cell, as shown in Fig. 3-6 and 3-2, respectively. Interestingly, this is the case from a very early stage of the operation when the nanoporous

Pt of the BP cell is not expected to have developed significant agglomeration. This indicates that the effect of suppressed agglomeration only cannot fully explain the oxide-overcoat-induced enhancement of ORR kinetics. In Fig. 3-7c, the two electrode resistances of the CP cell at t = 1 h exhibit different $p(O_2)$ dependences as those of the BP cell did. The processes characterized by R_2/CPE_2 and R_3/CPE_3 have reaction orders of m = 0.844 (close to 1.0) and 0.034 (close to 0), respectively. Overall, the R_3/CPE_3 process dominates R_2/CPE_2, especially above 0.2 atm of oxygen.

First, the R_2/CPE_2 process is likely to correspond to a process involving molecular O_2 species such as O_2 adsorption as reported in a recent ORR mechanism study for ultrathin ZrO^{2-}coated Pt by Liu et al.(25) On the other hand, the very small m value of the R_3/CPE_3 process can be ascribed to the incorporation of oxide ions (O^{2-}) into the vacancies of electrolyte or gaseous O_2 diffusion on the surface of Pt.[136], [139]–[141], [143] If the ORR rate is governed by O_2 diffusion, R_{ct} is not expected to show an explicit temperature dependence. As the CP cell shows an Arrhenius behavior with the activation energy of 1.26 eV at OCV and 1.14 eV at n = 0.3 V (Fig. 3-8), it is reasonable to ascribe the process with m = 0.034 to the charge incorporation process.

Alternatively, the following scenario is possible for the CP cell. An ultrathin layer of YSZ partially covers pt, either in a well-connected network or in dispersed islands, the effective electrochemically active sites where Pt, air, and O^{2-} conducting channel meet altogether should have been enlarged significantly. The ionic species generated at these sites may travel through the newly formed Pt/YSZ interfaces, and this may be responsible for the activation energy of 1.14 eV. However, the ionic transport through the nano thin YSZ overcoat itself is likely negligible because the overcoat is very thin and probably not well-connected all of the way to the electrolyte interface. If the new Pt/YSZ interface became a new channel of O^{2-} transport, the distance through which the dissociated atomic species needed to travel on the Pt surface should be reduced significantly by the overcoat, making the overall ORR kinetics much facilitated. This explanation is also well-aligned with the disappearance of the process with m=∼0.5 that used to be dominant in the BP cell.

The αn value quantified even from the steepest slope of Fig. 3-7c,d (between η = 0 and 0.2 V) was <0.15 for both 1 and 14 h data. Given the common α value of ~0.5, the resulting n is too small to correspond to the charge transfer process of ORR. It is noted that Fig. 3-8 is based upon the cell overpotential, not the activation overpotential. However, ohmic overpotential comprises <10% of the total cell overpotential even under the cell overpotential of 0.4 V and thus is not significant enough to affect the arguments discussed above.

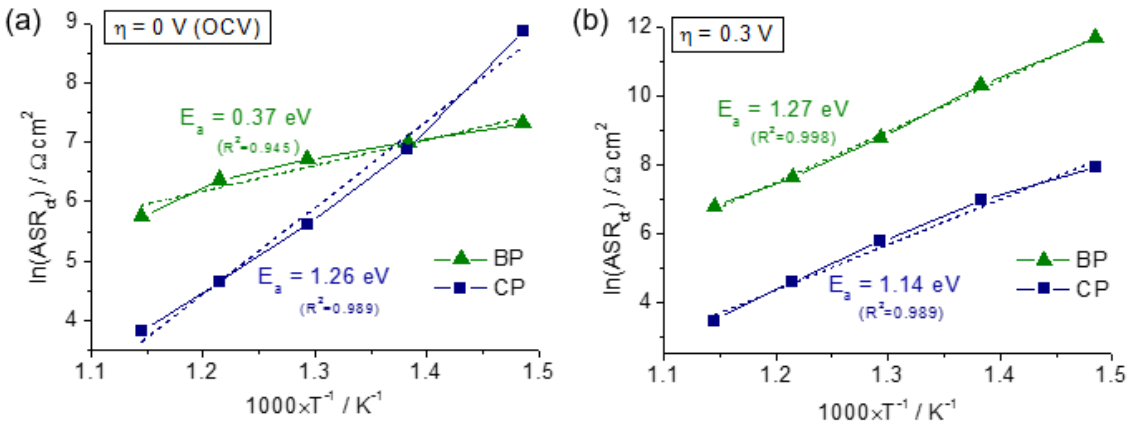

Fig. 3-8 Arrhenius plot of the BP and CP cells measured under (a) η = 0 V (OCV condition) and (b) η = 0. 3 V. The measurements were performed at 400, 450, 500, 550, and 600 °C in the decreasing sequence after the cells were exposed to 600 °C for 14 h.

The observations mentioned above can be summarized as follows. First, in our BP cell, a chemical potential-driven process mediated by atomic oxygen species is the limiting process in ORR when the Pt electrode is relatively intact (at t = 1 h). The bottleneck process is probably dissociation of oxygen molecules into atoms and/or surface transport of oxygen atoms. As agglomeration continues during the operation at 600 °C, the site for charge transfer reaction (i.e., TPB) will become significantly smaller, which is further supported by the morphology images shown in Fig. 3-2, making the overall ORR kinetics limited by a charge transfer-related step. As for the CP cell, the ORR is initially governed by both O^{2-} incorporation into the electrolyte lattice and a chemical process, not being entirely dominated by either of the two processes. While the contribution of the former is somewhat more substantial than the other throughout the $p(O_2)$ of study, that of the latter becomes

larger with smaller $p(O_2)$. It is also noted the m = 0.48 trend appearing in the BP cell is not visible in the CP cell. This suggests that the oxygen dissociation process or atomic diffusion, which used to be the rate-limiting step in the BP cell, becomes highly facilitated by an ultrathin YSZ overcoat and does not play as the rate-limiting step in the CP cell.

3-3-3 Conclusions

It was reported earlier that a highly uniform nanoscale YSZ overcoat on a Pt catalyst enabled by ALD preserves the underlying Pt nanostructure and even enhanced the ORR kinetics significantly.[133] While the impact of overcoat on the Pt agglomeration seems obvious, it stayed mysterious that the CP cell showed a much higher ORR activity than the BP cell even when the bare Pt was not agglomerated. In this section, a systematic electrochemical analysis was presented to reveal the mechanism and suggest the following. First, the ORR kinetics on a current nanoporous Pt/YSZ system is mainly governed by an O^- mediated chemical process. After the Pt becomes highly agglomerated during high-temperature operation, the rate-limiting step shifted to the charge transfer reaction due to a much smaller TPB area. On the other hand, a nanoporous Pt catalyst with uniformly dispersed nanoscale YSZ overcoat seems to exhibit an ORR process mainly limited by the O^{2-} incorporation process while a chemical process also plays a considerable rate-determining role especially at a low pO_2 regime (< 0.1 atm). With these observations, the YSZ overcoat on Pt can be regarded as a significant facilitator of chemical processes related to non-charged oxygen species during ORR in addition to an effective suppressor of Pt agglomeration (Fig. 3-9).

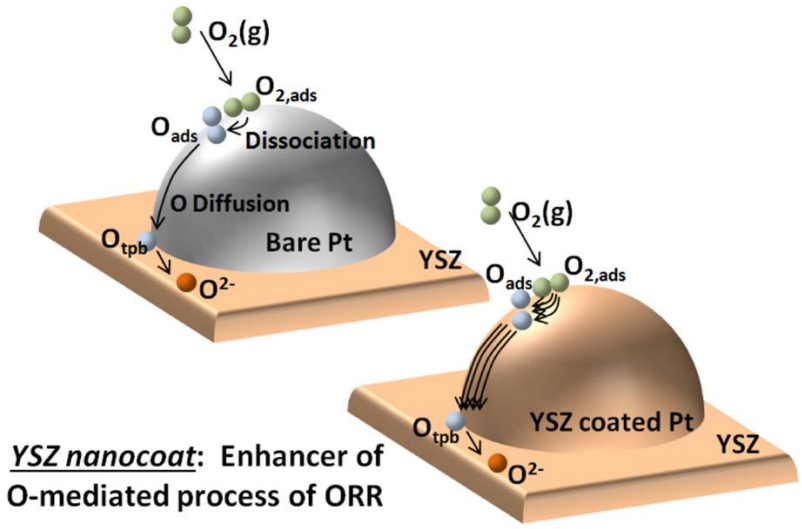

Fig. 3-9 Schematic of YSZ ALD impact on different components of ORR on Pt particle

Chapter 4 Effect of spin coating on the interface of LNF/GDC in SOFCs

4-1 Introduction

To improve solid oxide fuel cell (SOFC) technology, several steps have been made so far. Changing the nanostructure and nanocrystallinity of materials are one of these steps that helped improving material properties. To obtain the desired nanostructure, low-temperature deposition techniques such as spincoating, atomic layer deposition (ALD), or infiltration can be used. Cathode resistance has a high contribution to the total area specific resistance (ASR) of the fuel cell. Thus, strategies to lower the cathode resistance are needed. One of the methods to lower the cathode resistance is interfacing the cathode/electrolyte with the thin functional layer (FL) with methodes such as spincoating . Which allows modifying the nanostructure of this thin layer Spincoating is not only a cost-effective coating technique, but it also has a significant impact on reducing the resistance of the cathode.[168], [169]

To make cells more efficient, one crucial step besides lowering the cathode resistance is to have a better understanding of the cell's oxygen reduction reaction (ORR) mechanism. It will have a crucial impact on achieving a viable SOFC technology in the future. In this study, the effect of spincoated layers of $LaNi_{0.6}Fe_{0.4}O_{3-\delta}$ (LNF) and $LaNi_{0.6}Fe_{0.4}O_{3-\delta}Gd_{1-x}Ce_xO_{2-\delta}$ (LNFGDC) with a variety of thicknesses in the interface of LNF porous cathode and $Gd_{1-x}Ce_xO_{2-\delta}$ (GDC) interlayer have been examined and evaluated. The samples are prepared by a versatile and low-cost spincoating method on yttria-stabilized zirconia (YSZ) pallets. Spincoated layers are introduced on the interface of GDC interlayer and porous LNF cathode. X-ray diffraction (XRD) and scanning electron microscopy (SEM) have been used to find the properties of materials. Then symmetrical cells are tested by Electrochemical impedance spectroscopy (EIS) at different temperatures and oxygen partial pressures to have an advanced understanding of any change in the ORR mechanism and kinetics caused by introducing these spincoated layers.

4-2 Background of surface treatment approaches

Fuel cells are energy conversion systems that convert the chemical energy of hydrogen and fossil fuels directly into electrical energy. As a result of not being limited by the Carnot cycle, they are highly efficient and environmentally sustainable.[178]-[180] SOFCs are among the most promising types of fuel cells, which have been extensively researched as a very efficient source of electrical energy with the technical research history of the late 1930s when Emil Baur and H. Preis experimented materials such as zirconium, yttrium, cerium, lanthanum, and tungsten as a solid oxide electrolyte.

SOFCs typically consist of ceramic or cermet, porous electrodes separated by a dense ceramic membrane conductive to oxide ion, generally made of YSZ. The use of such materials indicates high temperature operation, which was one of the characteristics of SOFC. Traditionally high operating temperature SOFCs promote the kinetics of electrochemical reactions and charge transport through the ceramic components of the cell, which provided high power density in excess of 800 °C. However, despite certain apparent benefits, the widespread commercialization of this development has been greatly hampered by high costs, elevated thermal stress, lengthy startup and shutdown times and unintended chemical reactions between components of fuel cells.[181] Lowering the working temperature to medium temperature range (600–800 °C) is a key to avoid these issues which enable the long-term operation and hence the feasibility of this technology. However, reducing the operating temperature is correlated with a decrease in ion conductivity and a reduction in the catalytic activity of both electrodes.[182], [183]

It has been stated that the limiting factor in efficiency for the state-of-the-art fuel cells is the cathode overpotential. For cells measured at 700 °C, cathode overpotential contribution to a total ASR of anode supported SOFC dominates its performance as pointed out by Barfod et al.[184] As a result, the greatest improvement can be achieved by improving the cathode material. In the last few decades, persistent attempts have done to improve the ORR process, which is often the main source of power loss in reduced temperature SOFCs.

Cathode parameters such as composition, thickness, and microstructure have proven to strongly affect the electrochemical performance of SOFC. Thus, extensive work has been performed on the quest for novel cathode materials with favorable overall properties at temperatures below 800 °C.[185] –[187] Besides the cathode's proper chemical composition, it is also necessary to change the microstructure properly, particularly at the interface between the cathode and the electrolyte.[188]–[189]

As a consequence, adding a film of at least 10 μm thick cathode functional layer, which has a finer microstructure than a conventional cathode current collector layer (CCL), began a standard procedure. Tanner et al.[191] also showed another theoretically proven justification for such a layer. Rieu et al.[192] used dipcoating to prepare a thin film of 2 μm thick and Woolley et al.[193] recorded using screen printing to obtain a 5 μm thick FL, which reduced the polarization resistance of $La_2NiO_{4+\delta}$ cathode. Lee et al.[194] reported that due to the enhanced oxygen ion incorporation rate at the cathode/electrolyte interface, the interfacial ASR of $SrTi_{0.65}Fe_{0.35}O_{3-\delta}$ (STF)/ GDC cathodes on a GDC electrolyte was significantly reduced compared to that of the same cathode on a YSZ electrolyte.

Since then, much thinner functional layers between the cathode/ electrolyte have been found to improve the performance of the fuel cells. Enhancements in the properties of SOFC cathode components can be accomplished by modifying the nanostructure of this thin layer utilizing various deposition techniques such as pulsed laser deposition (PLD), spin coating, and spray pyrolysis which offers the possibility to form thin ceramic coatings with nanocrystalline grain size at low temperatures. Hildenbrand et al.[169] reported an increase in the mechanical stability and ionic conductivity of the cathode/electrolyte interface for $La_{0.6}Sr_{0.4}Co_{0.2}Fe_{0.8}O_{3-\delta}$ (LSCF) and $La_2NiO_{4+\delta}$ (LNO) cathodes through utilizing a thin dense layer produced by PLD. Despite the fact that the PLD provides high quality ceramic layers, its high level of technical sophistication and high cost make it difficult to use in large scale production. Setevich et al.[188] studied the potential usage of polymeric precursor spin coating to achieve dense layers. They synthesised and characterized the impact of 700 nm thick LSCF spincoated layer between the GDC electrolyte and the LSCF cathode.

Chrzan et al.[174] examined the effect of functional layer sintering temperature on the cathode performance. They deposited a thin (∼140 nm) spincoated perovskite layer of LSCF between a cathode LSCF and an electrolyte GDC and the effects of this investigated. They changed the sintering temperature to vary the micro-structure of this layer in order to determine its impact on the electrical and electrochemical properties. It has been shown that a mesoporous, nanocrystalline layer increases the active area for oxygen reduction and charge transfer through the cathode/electrolyte interface, which improves performance. Moreover, the stability of the cathode from thermal stresses is increased. In contrast, the coarsening of the grain and the layer densification has a negative impact on the cathode performance.

In another analysis by Chrzan et al.[195], thin functional layers made of three different perovskites, LNF, $SrTi_{0.65}Fe_{0.35}O_{3-\delta}$ (STF) and LSCF with various thicknesses (from 30 nm to 440 nm) were deposited to boost the cathode performance. Evans et al.[196] spincoated LSC with a thickness of 250 nm as a cathode on micro SOFCs which are miniaturized fuel cells using sub micrometer thick ceramic electrolyte membranes. Zhao et al.[197] deposited LNO electrodes on a solid substrate of $Ce_{0.8}Sm_{0.2}O_{1.9}$ electrolyte by a spincoating technique and found out the polarization of surface oxygen exchange process was the major contributor to the total electrode polarization.

Giuliano et al.[198] investigated the effect of electrode/electrolyte interface structure on the performance of $Pr_{0.8}Sr_{0.2}Fe_{0.7}Ni_{0.3}O_{3-\delta}$ (PSFN8273) as SOFC cathode. They introduced GDC interlayer on the PSFN8273 cathode on two different symmetrical half-cells, with dense GDC electrolyte pellet (GDC/PSFN cell) and with GDC interlayer deposited on YSZ pellet (YSZ) (YSZ/GDC/PSFN cell). After fitting the EIS data using an adapted equivalent circuit (EC), they found out polarization resistance (R_p) is higher for the YSZ/GDC/PSFN cell compared to the GDC/PSFN cell. They concluded that this increase is assigned to the difference in their interface microstructure. Besides, the long-term stability is evaluated through an aging test applying a current density of 123 $mAcm^{-2}$ for 1000 h at 700 °C in air that revealed PSFN8273 was an stable material for SOFC cathode. These results mean that even if the GDC interlayer affects the cathode

performance (in terms of R_p), it did not influence its stability, making PSFN8273 a suitable material as cathode for SOFC application.

Molin et al.[199] found out the introduction of the thin FL between the cathode and the electrolyte by spincoating has led to the lowering of the ASR of the oxygen electrode by ∼24%. They concluded that a critical contribution of the layer is improving contact between the electrolyte and the porous cathode. On the other work, Molin et al.[200] used a spray pyrolysis method to deposit thin cathode functional layers based on the $LaNi_{0.6}Fe_{0.4}O_3$ (LNF) material. They deposit thin layers of $Ce_{0.8}Gd_{0.2}O_2$ and LNF between the electrolyte and the porous oxygen electrode. Testing of symmetrical fuel cells shows a clear improvement of the electrochemical processes, resulting in lower polarization resistances allowing for higher power fuel cells. Their cathode resistance decreased more than 17 times, from 1.6 Ω cm^2 to less than 0.1 Ω cm^2 at 800 °C. They reported that the introduction of the new thin functional layers between the electrolyte and the porous electrode seems to be very beneficial in terms of the reported performance. However, they did not analyze this impact to find the ORR process.

Baque et al.[201] studied a symmetrical cell composed of LSCF cathodes deposited on a $Ce_{0.8}Y_{0.2}O_{2-\delta}$ (CYO) substrate fabricated by the spincoating technique. They reported that electrolyte grain boundary conductivity strongly depends on cathode nature. The detailed high-resolution transmission electron microscopy (HR-TEM) characterization of the LSCFO/CYO interface revealed that the LSCFO cathode well adheres to the CYO electrolyte. They reported that improved nano/microstructure of the cathodes and the cathode/electrolyte interface yields to ASR_{ct} values as low as 0.4 Ω cm^2 at 550 °C and concluded such low ASR values are a result of the optimal cathode nanostructure along with the well-adhered cathode/electrolyte interface which facilitates the oxygen ion transfer from cathode to the electrolyte.

Previous research centered more on cathodes with strong ion conductivity and thick layers constructed of the same material. It is, therefore, necessary to investigate the impact of a thin perovskite layer on the properties of the cell with primary electronically conductive cathode material. Despite the previous works, the efforts on the electrochemical properties of thin spincoated LNF based cathodes in relation to the thickness remains

inadequate towards the difference of thin MIEC or electron conductor FL. As has been stated, the electrochemical properties of a cathode operating on an electrolyte are highly dependent on the cathode microstructure, grain size, porosity, cathode/ electrolyte triple-phase boundary length and the adherence of the cathode to the electrolyte. The mechanism of the increase in the cathode activity is not yet well known. Thus, the effect of the spincoated layer on the LNF cathode has yet to be evaluated. None of the reports so far conducted a test to carefully examine the impact of the spincoated layer with respect to its ion conductivity and thickness; This is addressed in this paper. Namely, LNF cathodes with two different thin perovskite of LNF and LNFGDC which have contrasting ionic conductivity examined at variety of spincoated thickness at multiple temperatures. The hypothesis also examined with ALD and cathode infiltration. ALD coating of CeO_2 and YDC increases the available reaction cites in the cathode FL without making a ion conducting path to the electrolyte. Infiltration increases the number of triple phase boundaries on the porous cathode. Thus, we can examine the efect of increasing the TPBs inside the FL in comparison with the effect of FL spin coating.

4-3 Experimental and cell fabrication

Symmetrical cells consisted of YSZ electrolyte, GDC interlayer, spincoated functional layer, and LNF current collecting layer with the reaction area of 0.35 cm^2. The schematic of the cell can be seen in Fig. 4-1.

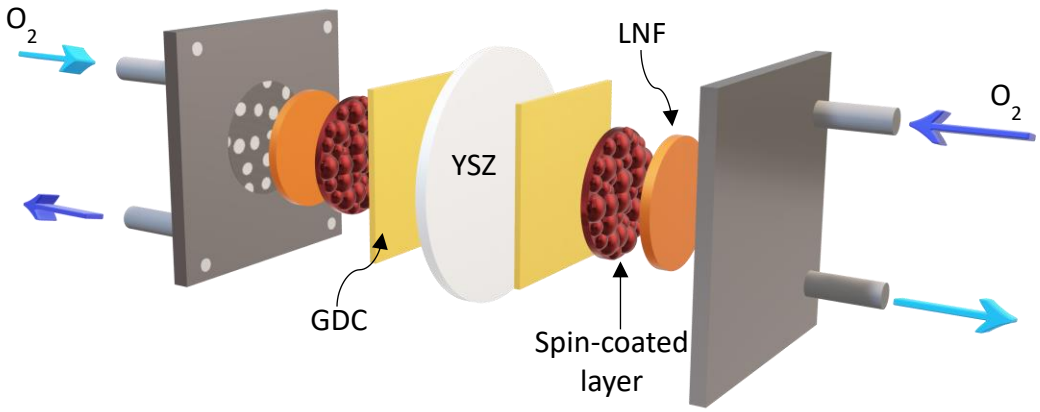

Fig. 4-1 Schematic of spincoated sample layers.

Each layer was sintered from slurry and screenprinted on the YSZ electrolyte layer by layer. YSZ electrolyte that used for this test was 8 mol% YSZ ($Y_{0.16}Zr_{0.84}O_{2-\delta}$) pellets (270 μm, FuelCellMaterials) as electrolyte supported substrates. For creating GDC slurry, GDC nanopowder (surface area: 30–40 m^2g^{-1}; d_{50} particle size: 0.1–0.4 μm; FuelCellMaterials) and ethyl cellulose were added and mixed at room temperature overnight. Final slurry was composed of 40 wt% terpineol, 10 wt% hypermer KD^{-1}, 2 wt% ethylcellulose, and 48 wt% GDC nanopowder. First, the GDC slurry screenprinted one time on both sides of the YSZ electrolyte. After that, GDC screenprinted samples dried at 80 °C for 1 h and then sintered at 1250 °C for 5 h. The samples were heated to 500 °C in 2 °Cmin^{-1} for sintering and held for 30 min at 500 °C to promote binder burning off. Samples continued to be heated to the sintering temperature of 1250 °C at 3 °Cmin^{-1}, and

after sintering, cooled down at 3 °C min^{-1} to room temperature. Such a high sintering temperature makes the GDC layer's surface less corrugated. Thus, the observation of the spincoated layer surface is more straightforward.

In the next step, a thin layer of LNF or LNFGDC deposited on both sides of samples using spincoating at 500 rpm for the 30 s followed by 1500 rpm for 20 s. After each step, samples dried at 100 °C for 2 min followed by a fast annealing on a hot plate at 500 °C for 1 min. LNF and LNFGDC solutions for spincoating were prepared from the stoichiometric amount of nitrate-based solutions with deionized water as a solvent. During the low rpm step, nitrate solution fully covers the surface. The high rpm spincoating step thins the spincoated layer. The spincoating process repeated until the desired thickness obtained. The average thickness of each spincoated layer was around 48 nm, based on the SEM images that are available for both LNF and LNFGDC. (Fig. 4-2 a-b)

To make LNF slurries for screenprinting, LNF powder was first synthesized with lanthanum (III) hexahydrate nitrate, nickel (II) hexahydrate nitrate, iron (III) nonahydrate nitrate, glycine, and deionized water. A weight ratio of 1:0.403:0.373 (La: Ni: Fe) nitrate precursors were dissolved in a minimum amount of deionized water while stirring on a hot plate. Glycine was gradually applied to the solution when mixing (with a weight ratio of 1:0.877 between the nitrate precursors and glycine), which turns the solution color into dark red. Once it was dissolved, the water evaporated at about 150 °C until the liquid became like glue. Then the combustion reaction process completed at 325 °C. The reaction product was broken into smaller clusters after cooling down and then calcined in a ceramic container at 850 °C for 3 h. The calcination changes the powder color from dark brown to pure black color scheme. For slurry, dispersant (Hypermer, Croda) was dissolved at 50 °C overnight in terpineol with a magnetic mixer, and 3 h of ethylcellulose and LNF powders were then applied to the mixture before ball-milling.

After spincoating, LNF current collecting layer screenprinted on both sides of spincoated cell that covered with 0.35 cm^2 circular mask. Then the sample dried at 80 °C

for 1 h, and another LNF screenprinting was performed on both sides of the cell. Then the sample calcinated at 500 °C, followed by sintering at 850 °C for 5 h.

4-4 Results and data analysis

Spincoating on the interface of GDC and porous screenprinted LNF has performed with 2 different materials: LNF and LNFGDC. The choice of LNF and LNFGDC is because of their significant differences in ionic conductivity, electronic conductivity, and electrochemical performance toward ORR. Since the cathode is made on a LNF backbone, we examine the impact of LNF and LNFGDC spincoating on the LNFcathode/GDC interlayer interface to have a clear conclusion about the impact of the spincoated layer on ORR performancein terms of ion conductivity and thickness. The thickness of spincoating varies between ~50- 500 nm for both sets of spincoating materials. Fig. 4-2 shows SEM images of LNF and LNFGDC spincoated samples. Samples with 10 layers of LNF and LNFGDC spincoating were chosen for SEM imaging to demonstrate the differences in thickness and porosity. The nanoparticle-like features of spincoated LNF and LNFGDC are clearly visible in the interface of GDC interlayer and porous LNF as shown in both Fig. 2a-b. images revealed that the average thickness of 10 layers is around 480 nm on both LNF and LNFGDC spincoated samples. Besides, the spincoated layers are denser than the screenprinted layers.

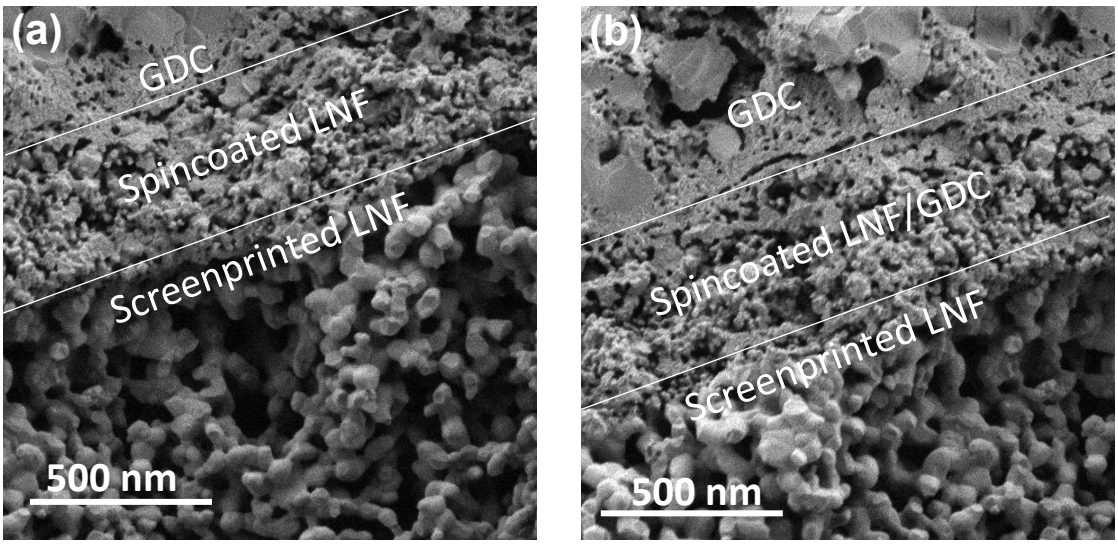

Fig. 4-2. SEM images of (a) spincoated LNF and (b)spincoated LNFGDC sample. The spincoating repeated10 times for both samples to achieve this thickness. The scale bars correspond to 500 nm.

XRD analyses were also performed to determine the phases additionally formed by the spincoating process. While a different number of spincoated layers was performed for electrochemical characterization presented below, ten steps of spincoating were performed for XRD characterization purposes of acquiring reliable diffraction spectra of infiltrated materials. The subsequent XRD spectra (Fig. 4-3) reveals that the backbone LNF was found to comprise predominantly of rhombohedral crystals with a slight amount of the form $LaNiO_3$ Phase. The LNF spincoated sample exhibits an intense peak that corresponded to La_2NiO_4, a Ruddlesden-Popper (RP) phase. It also showed an additional peak relating to orthorhombic $LaFeO_3$ at $2\theta = 61.2°$, whereas all other peaks coincide with those of backbone LNF. While in the LNF spincoated sample the intended nominal stoichiometries of the backbone and the overcoat (the spincoated layers) are the same, the difference in the synthesizing process of backbone and overcoat (mechanical pressing of backbone powder; sol impregnation for overcoat) may have caused the difference in the secondary phase. In the LNFGDC spincoated sample, additional GDC peaks observed. However, peaks linked to the secondary phases of La_2NiO_4 and $LaFeO_3$ were not detect.

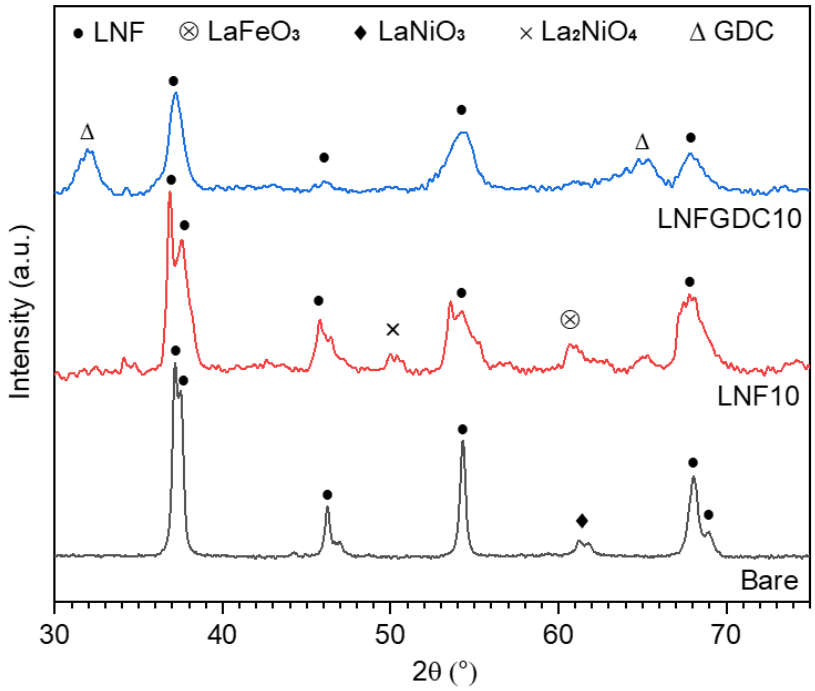

Fig. 4-3 XRD spectra of bare and spincoated LNF substrates.

The impact of the spincoating thickness of LNF and LNFGDC nitrite precursors was then studied, increasing the amount of coating from 1 to 10 layers and 15 layers, respectively. The equivalent circuit shown in Fig. 4-4a is used to extract the ohmic resistance (R_O) and electrode polarization resistances (R_H, R_M, and R_L, corresponding to high, medium and low frequency arcs, respectively). Fig. 4-4 b-d display impedance spectra of symmetric bare and spincoated samples obtained in the open circuit condition at 700°C. Note that the presented resistance values are normalized by cell area (0.35 cm^2). For each Nyquist plot, the x-intercept of the high frequency regime corresponds to the cell's ohmic resistance, whereas the arc-like characteristics are attributed to electrode polarization. The ohmic resistance for both spincoated LNF and LNFGDC samples remains unchanged. The existence of inflections (i.e., variations in curvature) in the arcs suggests that the analysis catches several electrode processes. The Nyquist plots reveal the total arc size decreases significantly even with 50nm thickness of spincoating for both LNF and LNFGDC spincoated samples.

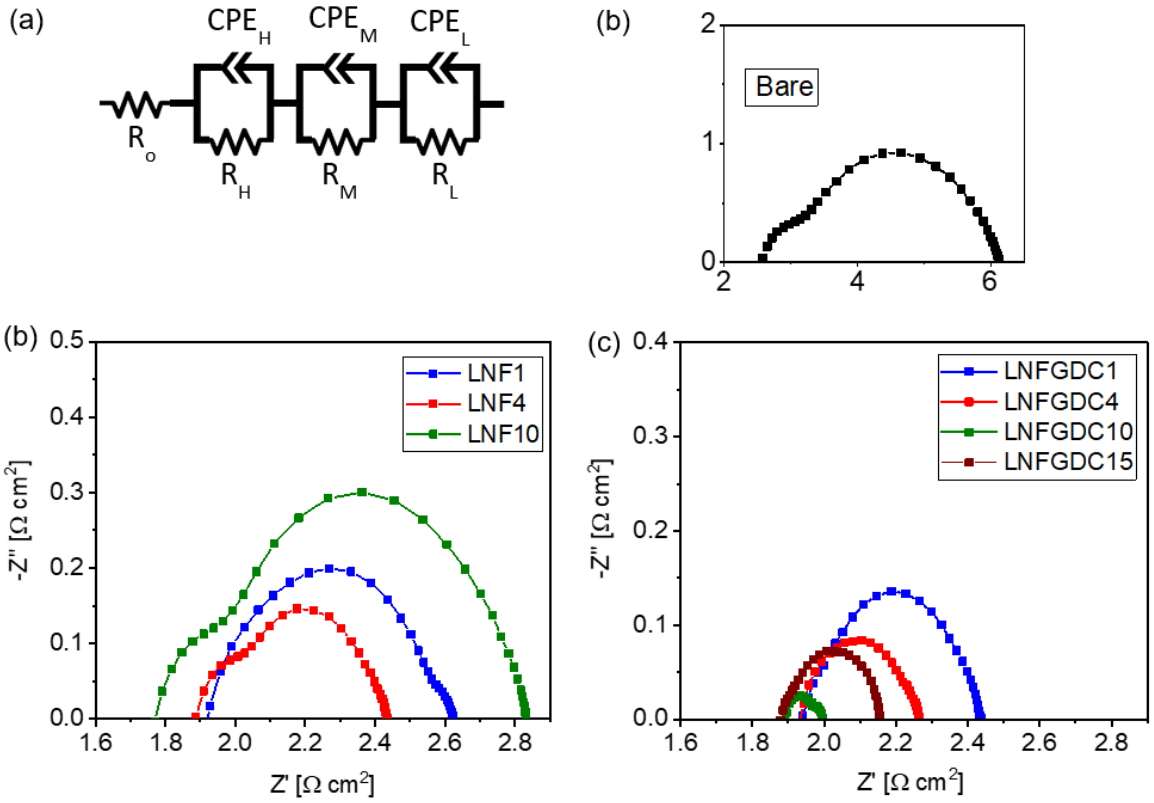

Fig. 4-4 (a) Equivalent circuit used to model the system, Nyquist plots of (b) Bare, (c) LNF spincoated, and (d) LNFGDC spincoated samples, obtained under the open circuit condition at 700 °C.

In Fig. 4-5, the fitted R_M values are presented based on the number of spincoated layers of LNF and LNFGDC. Interestingly, R_M values are always higher than R_L for all the samples at 700 °C. Based on this finding, Fig. 4-5 focuses on R_M relevant to the bottleneck mechanism in the examined samples. The optimal thickness of the spincoated layers for electrode performance is observed to be mostly above 200 nm for both LNF and LNFGDC interlayers, whereas the polarization arc increases by growing the thickness to about 500 nm.

It is also clearly shown that polarization resistance values shrunk significantly, after a single-step spincoating on the interface of GDC interlayer/ porous LNF cathode, regardless of the spincoated material, revealing the crucial impact of cathode/electrolyte nano-functionalization by spincoating on improving air electrode efficiency. Table 4-1

reports a description of the polarization resistances and capacitance elements (C) obtained from each LNF and LNFGDC spincoated cells at 700 °C.

It is noticed that even the spincoating of LNF, the same substance as the backbone, also greatly decreased the polarization resistance (R_p) by more than 7 times (from 3.6 to 0.5 Ω cm^2) at 700 °C. Here, $R_p = (R_H + R_H + R_L)/2$ where each symmetric cell has a division by 2 to account for one of the two electrodes as the only significant distinction between the spincoated and bare LNF samples is the nanostructured spincoated LNF in the LNF/GDC interface which has 3 - 4 times smaller LNF crystals on average than the screenprinted LNF.

This indicates that an increase of actual cathode functional layer surface area has a vital role in the overall ORR performance of this system. However, a possible discrepancy in the surface-specific chemical states between the two cannot be entirely ruled out at this stage. The XRD analysis alluded to the above showed that unlike the bare sample, the LNF spincoated sample has a slight orthorhombic $LaFeO_3$ phase. The fact that $LaFeO_3$ is inert towards ORR nevertheless upholds the influence of surface area on the overall ORR kinetics of LNF.

The best ORR performance was obtained with 10 layers of LNFGDC spincoating corresponding to ~480 nm, exhibiting R_p ~0.1 Ω cm^2 at 700 °C, a 36-fold improvement over the non-spincoated cell. This is attributed to the outstanding ORR performance of LNFGDC composite due to the excellent LNF electron conductivity and decent GDC particle ion conductivity that helps to make LNFGDC an MIEC cathode in contrast to LNF.

The thickness variation also gives us important data about the impact of spincoating on LNF (as an electron conductor cathode) and LNFGDC (as an MIEC cathode). On spincoated LNF samples, increasing the thickness from ~50 to ~200 nm does not have a noticeable impact on R_M. However, in spincoated LNFGDC cells, R_M continuously decreases to more than 5 times by increasing the thickness to ~500 nm spincoating. It shows increasing the amount of available sites for dissociative adsorption has an enormous impact in terms of cathode resistance on LNFGDC as an MIEC cathode. However, the beneficial

effect cannot be found in the case of LNF interlayer since the oxygen ions far from the GDC layer cannot transfer to the electrolyte due to the poor ionic conductivity of LNF.

It is also noticeable that by increasing the thickness of spincoating to ~500 nm in LNF and ~750 nm in LNFGDC, R_M increases and peak frequency shifts to lower frequencies. Both of them are considered to signify the blockage of oxygen access to the FL surface.

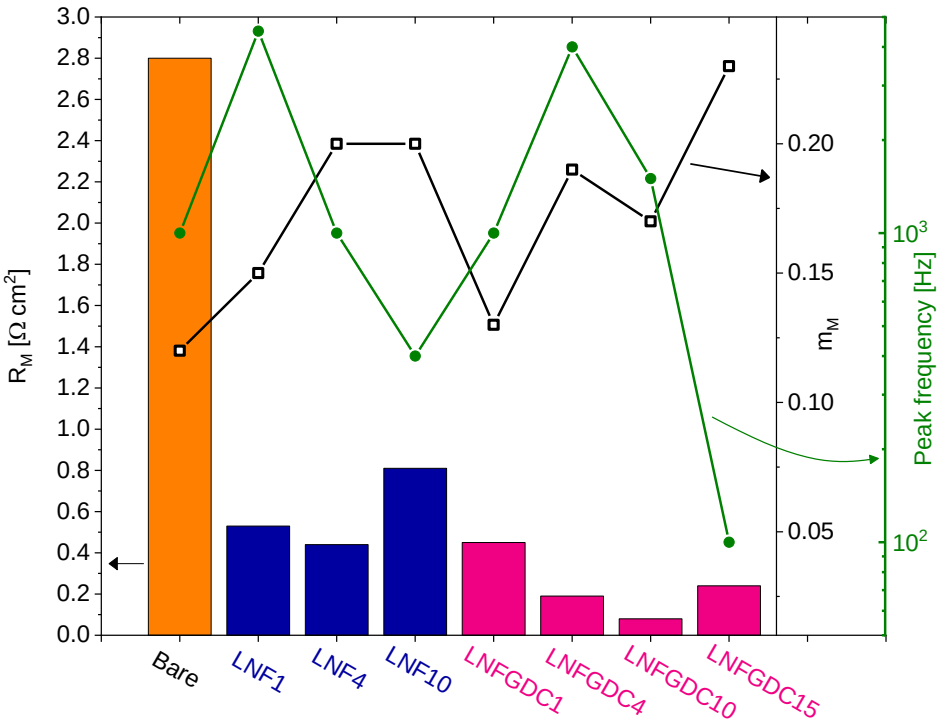

Fig. 4-5. R_M values on the left scale bar and m_M , peak frequencies on the right scale bar for bare, LNF, and LNFGDC spincoated samples with thickness variation.

Table 4-1 Ohmic resistance (R_o), polarization resistances from high frequency (R_H), medium frequency (R_M) and low frequency (R_L) arcs, and capacitance values (C_H , C_M, and C_L) of bare and spincoated samples obtained at 700 °C (open circuit condition). The EIS data shown in Fig. 4b-d were used to fit the data.

	R_o [Ω cm^2]	R_H [Ω cm^2]	C_H [F cm^{-2}]	R_M [Ω cm^2]	C_M [F cm^{-2}]	R_L [Ω cm^2]	C_L [F cm^{-2}]
Bare	2.54	0.79	5.75×10^{-6}	2.8	1.62×10^{-4}		
LNF1	1.93	0.1	6.49×10^{-5}	0.53	1.43×10^{-4}	0.06	0.21
LNF4	1.89	0.15	1.08×10^{-4}	0.39	9.33×10^{-4}		
LNF10	1.8	0.21	1.14×10^{-4}	0.81	1.45×10^{-3}		
LNFGDC1	1.95	0.08	1.42×10^{-4}	0.4	8.81×10^{-4}		
LNFGDC4	1.94	0.09	1.74×10^{-4}	0.19	8.55×10^{-4}		
LNFGDC10	1.89			0.08	1.42×10^{-3}	0.02	0.89
LNFGDC15	1.64	0.03	1.73×10^{-3}	0.24	1.10×10^{-2}		

The temperature dependency of electrode performances was also characterized by spincoated samples (Fig. 4-6). From the R_M and R_L values extracted from EIS measurements at 4 different temperatures (550, 600, 650, and 700 °C), the activation energies ($E_{a,M,}$ and $E_{a,L}$) were quantified for each sample. Since the amplitude of R_M values are more substantial than R_L in every sample, it is reasonable to assert that the medium-frequency process is generally limiting the overall ORR kinetics. It is also noted that an accurate extraction of R_L (shown in Fig. 6b) is elusive because R_L is much smaller than R_M values in most of the samples. For these reasons, the primary focus was made on R_M values when discussing the rate-determining step (RDS) and overall ORR kinetics. A significant decrease in $E_{a,M}$ was accomplished by all the studied materials of spincoating; the initial

$E_{a,M}$ without a spincoating was 1.71 eV, but spincoating renders significantly smaller $E_{a,M}$ values of 1.16–1.5 eV. Also, the LNFGDC spincoated cells had lower $E_{a,M}$ than LNF spincoated cells. (10 layers of LNFGDC spincoating presented the lowest $E_{a,M}$ of 1.16 eV among the tested cells.) Not only this reveals the significant advantage offered by the spincoating process for improved ORR kinetics, but it also suggests that the RDS of ORR is likely to have shifted by the spincoating.

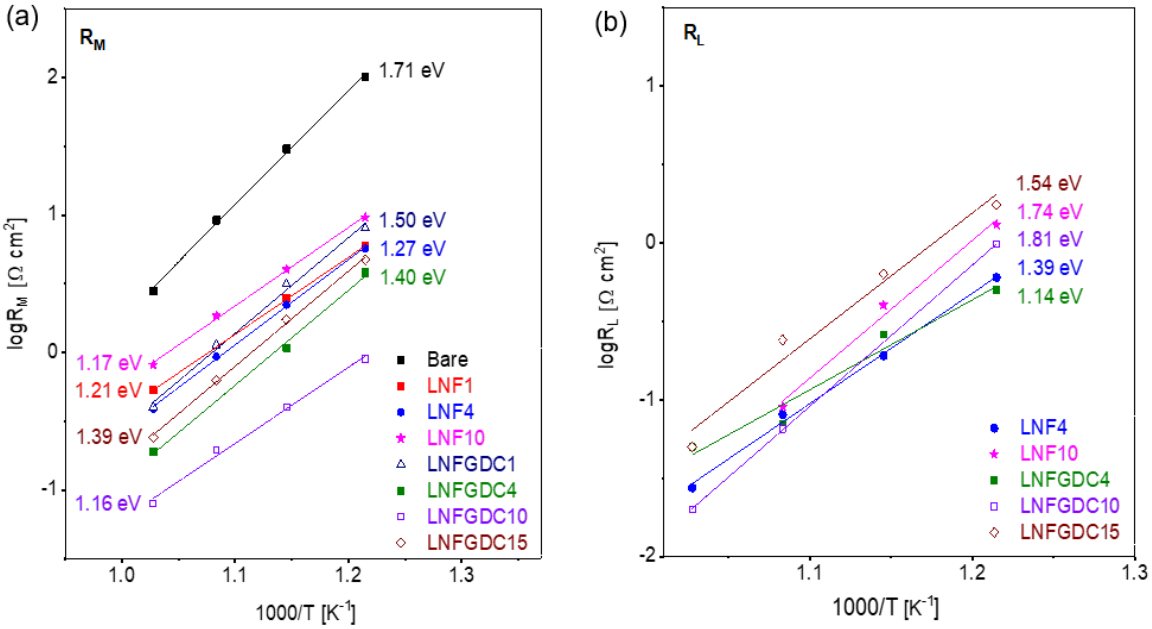

Fig. 4-6 Arrhenius plots of (a) R_M and (b) R_L based upon the EIS data of bare and spincoated samples obtained at 700 °C (open circuit condition).

After examining the spincoated cells with varying thicknesses of the LNF and LNFGDC, we performed supporting experiments to understand the change in ORR bottleneck by the interlayer. In the first supporting test, we prepared 10 layers spincoated LNF (LNF10) and 10 layers spincoated LNFGDC (LNFGDC10) samples and conducted a 1 time infiltration of 1M nitrate solution of LNF and LNFGDC on top of screenprinted LNF layer of each of those two types of samples, respectively. EIS results are presented in Fig. 4-7a. In the LNF10 sample that was infiltrated with LNF, no significant change was observed in EIS data at both medium and low frequency resistance range. Although this one-time infiltration had a significant impact on polarization resistance for the LNF sample

without the spincoated layer. The result confirms that 10 layers of spincoating are working as a functional layer for LNF cell since LNF has low ionic conductivity, and oxygen vacancies just near the GDC layer play an essential role in ORR kinetics. The top layer is just working as a current collector layer in this cell. By performing one-time infiltration of LNFGDC on the porous LNF at the LNFGDC10 sample, the polarization resistance increases by a factor of two. The peak frequency also shifted from medium frequency (3×10^3 Hz) to low frequency (25 Hz), as can be seen in Fig. 4-7b. These two facts together support the interpretation that 10 layers of LNFGDC spincoating can act as a full current collecting layer. The reasons are, first of all, the shift in a peak frequency from medium range to low range in this case which is a strong indication of blocking the oxygen availability on the functional layer. In addition, the infiltrated LNFGDC nanoparticles that attach to the porous screenprinted LNF although adding more available sites for oxygen adsorption, but the oxygen ion transform path to the GDC surface is too long. this lengthy ion conducting path increases the resistance which makes that available sites not efficient in the ORR process since the oxygen ions can not fast transform to the GDC interlayer. Thus, the 500 nm LNFGDC spincoated layer alone is enough for the cathode FL.

In the next step, the result of ALD YDC and ALD CeO_2 which have performed on LNF10 and LNFGDC10 samples compared with each other. ALD deposited on spincoated layer before applying the LNF screenprinted layer. EIS results (Fig. 4-7b) revealed that coating 1 nm and 2 nm of ALD YDC on the LNF spincoated samples makes R_p even increased it slightly. LNFGDC10 has more than 5 times lower total resistance than LNF10 samples with ALD coating. This result supports the hypothesis that dissociative adsorption is the bottleneck in LNF cathode since having 1-2 nm of ALD coating cannot provide an oxygen ion conductive path to the GDC interlayer. Therefore, the ALD YDC coating could not improve the ORR kinetics.

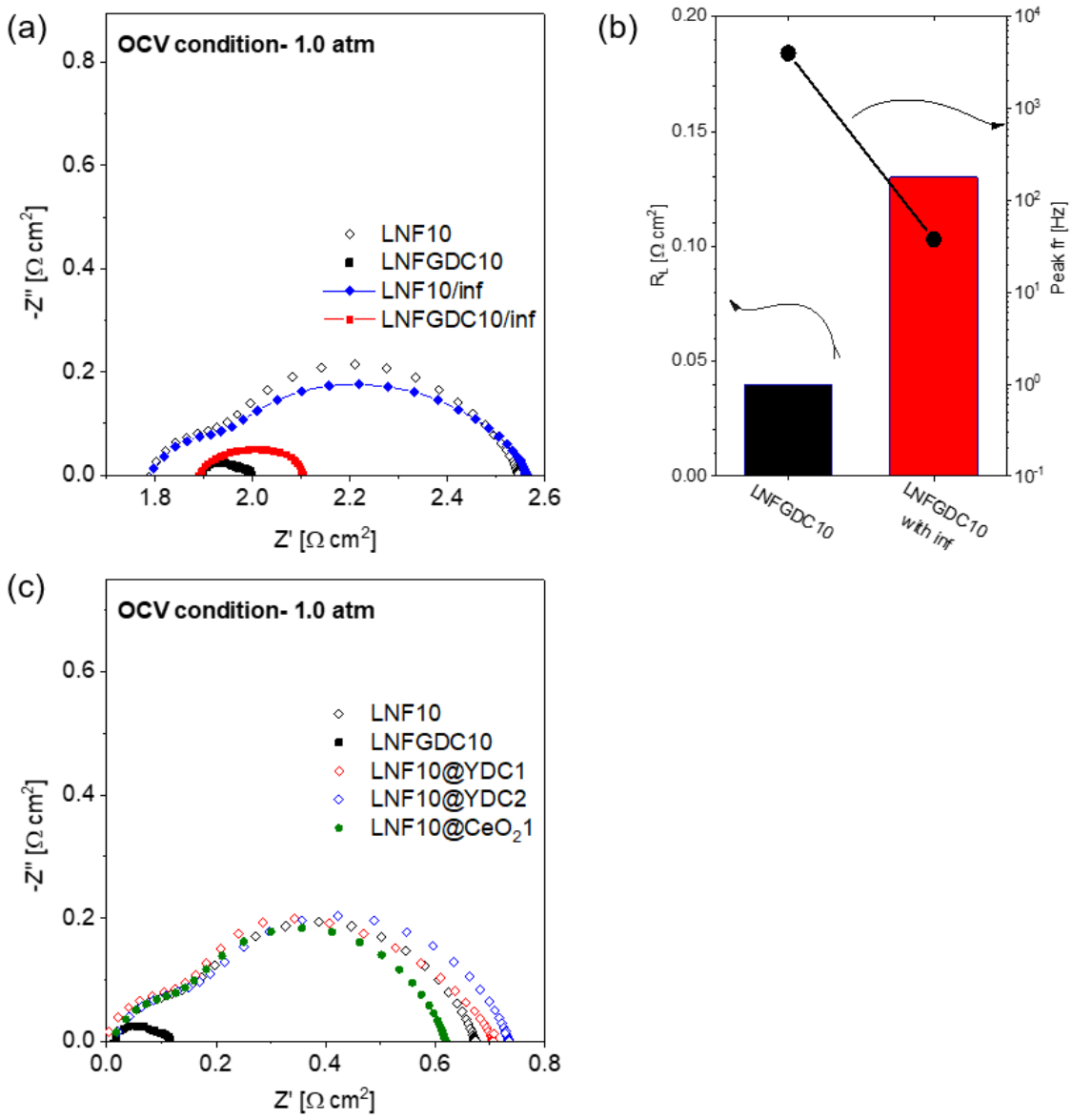

Fig. 4-7 (a) EIS plot of infiltration on spincoated samples, (b) R_L and peak frequency comparison on spincoated LNFGDC10 with and without LNFGDC infiltration, and (c) EIS plots of ALD coating on spincoated samples.

4-5 Conclusions

In this study, a critical impact of interfacial treatment by a spincoating process on the overall kinetics and RDS of ORR for LNF-based cells is demonstrated. Among all tested cells, the lowest electrode polarization resistance was achieved with LNFGDC spincoating with a thickness of ~480 nm, which corresponds to 10 layers of spincoating in the interface of GDC and LNF.

The XRD analysis revealed that all spincoated materials of choice were effectively crystallized by an 850 °C sintering process. Bare LNF's ORR kinetics are constrained by the surface process, most possibly dissociative adsorption, and partial oxygen reduction due to a deficient oxygen vacancy concentration.

The cathode polarization resistance substantially dropped by spincoating, which is ascribed to the enhancement of the surface process such as oxygen dissociation and surface diffiusion of oxygen or oxygen ions. Other important influences of ORR activity are the surface morphology and FL surface area, which is reinforced by the fact that spincoating of LNF (the same substance as the backbone) lowered the polarization resistance at 700 °C by more than 5 times.

Among the samples of study, LNFGDC10 spincoated cell showed the lowest polarization resistance of R_p = 0.1 Ωcm^2 at 700 °C in the open circuit condition, much smaller than the value from the bare LNF cell (R_P = 3.60 Ωcm^2). It is attributed to the LNFGDC nanocomposite MIEC properties, which increase the available cites for dissociative adsorption and the GDC ion conductive path to the surface of the GDC interlayer. Increasing the thickness proportionally increases the number of available sites for dissociative adsorption. For the LNFGDC interlayer-based samples, the oxygen ion generated in the higher spincoated layers far from the cathode/electrolyte interface can still be transferred to the GDC surface due to the high ionic conductivity of LNFGDC. However, in the samples with a LNF interlayer, the ionic transfer rarely occurs for sites far from the GDC surface due to the poor ionic conductivity of LNF material. For this reason, while a single layer spincoating of LNF and LNFGDC does not exhibit a significant difference in performance, for samples with a larger number of spincoated layers, polarization resistance of LNFGDC spincoated cell show a prominent advantage. All the

cells including the bare LNF cell exhibits an electron transfer-limited process in addition to dissociative adsorption-limited behavior.

Chapter 5- Summary

SOFCs are electrochemical engines that convert chemical energy into electricity. Compared to other types of fuel cells, SOFCs are advantageous in terms of efficiency and fuel flexibility. However, their high temperature working condition, which is conventionally above 1000 °C, is the cause of multiple major drawbacks including slow startup/shut-down, material cost, durability and reliability concerns. To avoid these undesired issues, many efforts have been made to lower the operating temperature. However, it comes with a different set of challenges because of more sluggish catalytic activities, lowered ionic conductivity and resulting in more inferior power density at low temperatures. A possible solution to these challenges can be found in nanoscale engineering of electrode and electrolyte materials. Nanotechnology offers numerous opportunities in the SOFC field to address both performance and durability issues.

The first challenge of IT-SOFC is in the development of suitable electrode materials with high electronic and ionic conductivity operating the lowered temperature regime. The electronic and ionic conductivity of cathode materials is primarily affected by the sintering process. While a high surface area is desired to compensate for a lowered electrochemical kinetics for low-temperature operation, the average temperature for electrode sintering would tend to agglomerate the electrodes with a high surface area. A sintering aid is expected to improve the sintering behavior of electrode materials at lowered sintering temperatures. Sintering aids also allow co-sintering of different layers in a cell. In the first project, the effect of sintering aid (specifically, cobalt oxide) was studied on the performance and microstructure of LSCF-based cathodes. By performing a systematic test, it was found that 1) the ohmic and electrode polarization resistances are highly coupled with the change of Co_3O_4 content; 2) Co_3O_4 content has significant impact on charge transfer kinetics on the FL while having moderate impact on electron transport in CL; 3) a selective application of sintering aid to a specific layer(s) can be considered for a better performance and durability.

Another common problem of SOFCs is the durability of electrode material in a prolonged operational condition. This is more important in the cathode side since its polarization resistance is a significant part of total resistance. Nano surface treatment of electrodes by ALD can be used to resolve this issue. A coating of a few nanometers of metal oxide on the cathode FL not only suppresses agglomeration of the porous cathode but also facilitate ORR kinetics. To better understand the mechanism of the ALD catalysis enhancement effect on Pt cathode, we conducted a series of electrochemical measurements at different temperatures, overpotentials, and oxygen partial pressures. These experiments revealed that the ORR kinetics on a new nanoporous Pt/YSZ system is mainly governed by an atomic-oxygen-mediated chemical process. However, after a short time at 600 °C, the rate-limiting step shifted to the charge transfer reaction due to a much smaller TPB area. On the other hand, a nanoporous Pt catalyst with a well-dispersed nanoscale YSZ overcoat seems to exhibit an ORR process mainly limited by the O^{2-} incorporation or O^{2-} transport through the new Pt/YSZ interfaces formed by the YSZ overcoat, whereas the molecular O_2 adsorption process also plays a considerable rate-determining role especially at a low $p(O_2)$ regime (< ~0.1 atm). These observations revealed that the YSZ overcoat on Pt could be regarded as a significant facilitator of chemical processes related to atomic oxygen species during ORR in addition to an effective suppressor of Pt agglomeration.

Another set of opportunities in advancing IT-SOFC technology can be found in the cathode/electrolyte interface. A set of spincoating on different materials with different thicknesses performed on YSZ/GDC symmetrical cell. To understand the impact of spin-coated layer on the interface of cathode/electrolyte, EIS data obtained at different temperetures and oxygen partial pressures. Beside SEM imaging and XRD, to support the hypothesis of ORR kinetics, infiltration and ALD coating also performed on different samples. We found out that spin-coated layer has smaller nanoparticle sizes and 3~4 times smaller nanocrystalinity that increase the active cites for dissosiative adsorption on the cathode side, comparing to the available cites on bare LNF. EIS data along with ALD coating also strongly support the hypothesis that ion conducting pass through the LNFGDC FL playes an important role in decreasing the polarization resistance comparing the bare

LNF cathode as well. IT helps the available cites not limited to the vicinity of GDC interlayer but be available inn entire FL and the ion transport to the GDC interlayer through GDC nanoparticles pathes.

To sum up, a combination of nanoscale treatments including cathode infiltration, metal oxide ALD coating, and cathode-electrolyte interface spin-coating pursued to achieve a significantly enhanced performance and durability by addressing the aforementioned issues. In addition, I also performed a systematic studies on the change in electrochemical kinetics and a possible shift of bottleneck process by the treatments to better understand the effect of each of this nano-functionalization on oxygen reduction catalysis process in SOFCs.

Bibliography

[1] E. T. A. Boudghene Stambouli, “Solid oxide fuel cells (SOFCs): a review of an environmentally clean and efficient source of energy,” *Renew. Sustain. Energy Rev.*, vol. 6, pp. 433–455, 2002.

[2] S. Singhal, “Advances in solid oxide fuel cell technology,” *Solid State Ionics*, vol. 135, no. 1–4, pp. 305–313, Nov. 2000.

[3] W. R. Grove, “XXIV. On voltaic series and the combination of gases by platinum,” *Philos. Mag. Ser. 3*, vol. 14, no. 86–87, pp. 127–130, Feb. 1839.

[4] W. C. Heraeus, “Über die elektrolytische Leitung fester Körper bei sehr hohen Temperaturen,” *Zeitschrift für Elektrotechnik und Elektrochemie*, vol. 6, no. 2, pp. 41–43, Jul. 1899.

[5] E. Baur and H. Preis, “Über Brennstoff-Ketten mit Festleitern,” *Berichte der Bunsengesellschaft für Phys. Chemie*, vol. 43, no. 9, pp. 727–732, Sep. 1937.

[6] M. Gasik, *materials for fule cells*. woodhead publishing, 2008.

[7] *Fuel Cell Handbook*. Inc, EG&G Services, 2004.

[8] J. Zhang, *PEM Fuel Cell Electrocatalysts and Catalyst Layers Fundamentals and Applications*. London: springer, 2010.

[9] M. Liu, M. E. Lynch, K. Blinn, F. M. Alamgir, and Y. Choi, “Rational SOFC material design: new advances and tools,” *Mater. Today*, vol. 14, no. 11, pp. 534–546, Nov. 2011.

[10] A. Evans, A. Bieberle-Hütter, J. L. M. Rupp, and L. J. Gauckler, “Review on microfabricated micro-solid oxide fuel cell membranes,” *J. Power Sources*, vol. 194, no. 1, pp. 119–129, Oct. 2009.

[11] A. Bieberle-Hütter *et al.*, “A micro-solid oxide fuel cell system as battery replacement,” *J. Power Sources*, vol. 177, no. 1, pp. 123–130, Feb. 2008.

[12] B. Steele*, “Materials for IT-SOFC stacks 35 years R&D: the inevitability of gradualness?,” *Solid State Ionics*, vol. 134, no. 1–2, pp. 3–20, Oct. 2000.

[13] A. D. James Larminie, *Fuel Cell Systems Explained, 2nd Edition*. John Wiley& Sons, 2003.

[14] S. J. Skinner and J. A. Kilner, “Oxygen ion conductors,” *Mater. Today*, vol. 6, no. 3, pp. 30–37, Mar. 2003.

[15] W. . Zhu and S. . Deevi, “A review on the status of anode materials for solid oxide fuel cells,” *Mater. Sci. Eng. A*, vol. 362, no. 1–2, pp. 228–239, Dec. 2003.

[16] V. A. C. Haanappel *et al.*, “Optimisation of processing and microstructural parameters of LSM cathodes to improve the electrochemical performance of anode-supported SOFCs,” *J. Power Sources*, vol. 141, no. 2, pp. 216–226, Mar. 2005.

[17] S. Singhal and K. Kendall, *High-temperature Solid Oxide Fuel Cells: Fundamentals, Design and Applications*. Elsevier Science, 2003.

[18] W. J. Quadakkers, J. Piron-Abellan, V. Shemet, and L. Singheiser, “Metallic interconnectors for solid oxide fuel cells – a review,” *Mater. High Temp.*, vol. 20, no. 2, pp. 115–127, Jan. 2003.

[19] N. MINH, “Solid oxide fuel cell technology?features and applications,” *Solid State Ionics*, vol. 174, no. 1–4, pp. 271–277, Oct. 2004.

[20] N. Minh and T. Takashi, “Science and Technology of Ceramic Fuel Cells,” *Comp. Educ.*, vol. 49, no. 3, pp. 374–387, Aug. 2013.
[21] S. P. Simner, M. D. Anderson, J. E. Coleman, and J. W. Stevenson, “Performance of a novel La(Sr)Fe(Co)O3–Ag SOFC cathode,” *J. Power Sources*, vol. 161, no. 1, pp. 115–122, Oct. 2006.
[22] A. Hammouche, E. Siebert, and A. Hammou, “Crystallographic, thermal and electrochemical properties of the system La1−xSrxMnO3 for high temperature solid electrolyte fuel cells,” *Mater. Res. Bull.*, vol. 24, no. 3, pp. 367–380, Mar. 1989.
[23] M. J. L. Østergård, C. Clausen, C. Bagger, and M. Mogensen, “Manganite-zirconia composite cathodes for SOFC: Influence of structure and composition,” *Electrochim. Acta*, vol. 40, no. 12, pp. 1971–1981, Sep. 1995.
[24] O. Yamamoto, “Perovskite-type oxides as oxygen electrodes for high temperature oxide fuel cells,” *Solid State Ionics*, vol. 22, no. 2–3, pp. 241–246, Jan. 1987.
[25] A. Petric, “Evaluation of La–Sr–Co–Fe–O perovskites for solid oxide fuel cells and gas separation membranes,” *Solid State Ionics*, vol. 135, no. 1–4, pp. 719–725, Nov. 2000.
[26] K. B. Prater, “Solid polymer fuel cell developments at ballard,” *J. Power Sources*, vol. 37, no. 1–2, pp. 181–188, Jan. 1992.
[27] H. Lv, B.-Y. Zhao, Y.-J. Wu, G. Sun, G. Chen, and K.-A. Hu, “Effect of B-site doping on Sm0.5Sr0.5MxCo1−xO3−δ properties for IT-SOFC cathode material (M=Fe, Mn),” *Mater. Res. Bull.*, vol. 42, no. 12, pp. 1999–2012, Dec. 2007.
[28] S. Wang and Y. Zou, “High performance Sm0.5Sr0.5CoO3–La0.8Sr0.2Ga0.8Mg0.15Co0.05O3 composite cathodes,” *Electrochem. commun.*, vol. 8, no. 6, pp. 927–931, Jun. 2006.
[29] J.-M. Bae and B. C. H. Steele, “Properties of Pyrochlore Ruthenate Cathodes for Intermediate Temperature Solid Oxide Fuel Cells,” *J. Electroceramics*, vol. 3, no. 1, pp. 37–46, 1999.
[30] H.-C. Yu and K.-Z. Fung, “Electrode properties of La1−xSrxCuO2.5−δ as new cathode materials for intermediate-temperature SOFCs,” *J. Power Sources*, vol. 133, no. 2, pp. 162–168, Jun. 2004.
[31] L. Tai, “Structure and electrical properties of La1 − xSrxCo1 − yFeyO3. Part 2. The system La1 − xSrxCo0.2Fe0.8O3,” *Solid State Ionics*, vol. 76, no. 3–4, pp. 273–283, Mar. 1995.
[32] L. Ge, W. Zhou, R. Ran, Z. Shao, and S. Liu, “Facile autocombustion synthesis of La0.6Sr0.4Co0.2Fe0.8O3−δ (LSCF) perovskite via a modified complexing sol–gel process with NH4NO3 as combustion aid,” *J. Alloys Compd.*, vol. 450, no. 1–2, pp. 338–347, Feb. 2008.
[33] H. Zhao, W. Shen, Z. Zhu, X. Li, and Z. Wang, “Preparation and properties of BaxSr1−xCoyFe1−yO3−δ cathode material for intermediate temperature solid oxide fuel cells,” *J. Power Sources*, vol. 182, no. 2, pp. 503–509, Aug. 2008.
[34] G. Kostogloudis, “Chemical reactivity of perovskite oxide SOFC cathodes and yttria stabilized zirconia,” *Solid State Ionics*, vol. 135, no. 1–4, pp. 529–535, Nov. 2000.
[35] Q. Xu, D. Huang, W. Chen, F. Zhang, and B. Wang, “Structure, electrical

conducting and thermal expansion properties of Ln0.6Sr0.4Co0.2Fe0.8O3 (Ln=La, Pr, Nd, Sm) perovskite-type complex oxides," *J. Alloys Compd.*, vol. 429, no. 1–2, pp. 34–39, Feb. 2007.
[36] S. Zhang, L. Bi, L. Zhang, C. Yang, H. Wang, and W. Liu, "Fabrication of cathode supported solid oxide fuel cell by multi-layer tape casting and co-firing method," *Int. J. Hydrogen Energy*, vol. 34, no. 18, pp. 7789–7794, Sep. 2009.
[37] P. Plonczak, M. Gazda, B. Kusz, and P. Jasinski, "Fabrication of solid oxide fuel cell supported on specially performed ferrite-based perovskite cathode," *J. Power Sources*, vol. 181, no. 1, pp. 1–7, Jun. 2008.
[38] S. Wang, "High temperature properties of La0.6Sr0.4Co0.8Fe0.2O3−δ phase structure and electrical conductivity," *Solid State Ionics*, vol. 159, no. 1–2, pp. 71–78, Mar. 2003.
[39] H. Tu, "Ln0.4Sr0.6Co0.8Fe0.2O3−δ (Ln=La, Pr, Nd, Sm, Gd) for the electrode in solid oxide fuel cells," *Solid State Ionics*, vol. 117, no. 3–4, pp. 277–281, Feb. 1999.
[40] L. Ge, R. Ran, Z. Shao, Z. H. Zhu, and S. Liu, "Low-temperature synthesis of La0.6Sr0.4Co0.2Fe0.8O3−δ perovskite powder via asymmetric sol–gel process and catalytic auto-combustion," *Ceram. Int.*, vol. 35, no. 7, pp. 2809–2815, Sep. 2009.
[41] W. Zhou, Z. Shao, R. Ran, H. Gu, W. Jin, and N. Xu, "LSCF Nanopowder from Cellulose–Glycine-Nitrate Process and its Application in Intermediate-Temperature Solid-Oxide Fuel Cells," *J. Am. Ceram. Soc.*, vol. 91, no. 4, pp. 1155–1162, Apr. 2008.
[42] K. Zhao, Q. Xu, D.-P. Huang, M. Chen, and B.-H. Kim, "Microstructure and electrode properties of La0.6Sr0.4Co0.2Fe0.8O3-δ spin-coated on Ce0.8Sm0.2O2−δ electrolyte," *Ionics (Kiel).*, vol. 17, no. 3, pp. 247–254, Apr. 2011.
[43] F. Zhao, Z. Wang, M. Liu, L. Zhang, C. Xia, and F. Chen, "Novel nano-network cathodes for solid oxide fuel cells," *J. Power Sources*, vol. 185, no. 1, pp. 13–18, Oct. 2008.
[44] J. M. Serra, S. Uhlenbruck, W. A. Meulenberg, H. P. Buchkremer, and D. Stöver, "Nano-structuring of solid oxide fuel cells cathodes," *Top. Catal.*, vol. 40, no. 1–4, pp. 123–131, Nov. 2006.
[45] D. Marinha, C. Rossignol, and E. Djurado, "Influence of electrospraying parameters on the microstructure of La0.6Sr0.4Co0.2F0.8O3−δ films for SOFCs," *J. Solid State Chem.*, vol. 182, no. 7, pp. 1742–1748, Jul. 2009.
[46] R. B. Yang., "Gas-phase synthesis of bismuth and antimony chalcogenide nano structures," *Ruhr-University Bochum*, 2010.
[47] M. K. Nicola Pinna, *Atomic Layer Deposition of Nanostructured Materials*. Wiley-VCH, 2012.
[48] X. Meng, "An overview of molecular layer deposition for organic and organic–inorganic hybrid materials: mechanisms, growth characteristics, and promising applications," *J. Mater. Chem. A*, vol. 5, no. 35, pp. 18326–18378, 2017.
[49] R. L. Puurunen, "Surface chemistry of atomic layer deposition: A case study for the trimethylaluminum/water process," *J. Appl. Phys.*, vol. 97, no. 12, p. 121301,

Jun. 2005.
[50] D. Gu *et al.*, “Precise control of highly ordered arrays of nested semiconductor/metal nanotubes,” *Nano Res.*, vol. 4, no. 2, pp. 164–170, Feb. 2011.
[51] C. F. Herrmann, F. H. Fabreguette, D. S. Finch, R. Geiss, and S. M. George, “Multilayer and functional coatings on carbon nanotubes using atomic layer deposition,” *Appl. Phys. Lett.*, vol. 87, no. 12, p. 123110, Sep. 2005.
[52] M. J. Weber, A. J. M. Mackus, M. A. Verheijen, C. van der Marel, and W. M. M. Kessels, “Supported Core/Shell Bimetallic Nanoparticles Synthesis by Atomic Layer Deposition,” *Chem. Mater.*, vol. 24, no. 15, pp. 2973–2977, Aug. 2012.
[53] P. Poodt *et al.*, “Spatial atomic layer deposition: A route towards further industrialization of atomic layer deposition,” *J. Vac. Sci. Technol. A Vacuum, Surfaces, Film.*, vol. 30, no. 1, p. 10802, Jan. 2012.
[54] V. Miikkulainen, M. Leskelä, M. Ritala, and R. L. Puurunen, “Crystallinity of inorganic films grown by atomic layer deposition: Overview and general trends,” *J. Appl. Phys.*, vol. 113, no. 2, p. 21301, Jan. 2013.
[55] J. Yuan, X.-Z.R., Song, C., Wang, H., Zhang, *Electrochemical Impedance Spectroscopy in PEM Fuel Cells*. London: springer, 2010.
[56] N. Mahato, A. Banerjee, A. Gupta, S. Omar, and K. Balani, “Progress in material selection for solid oxide fuel cell technology: A review,” *Prog. Mater. Sci.*, vol. 72, pp. 141–337, Jul. 2015.
[57] K. J. Yoon, P. Zink, S. Gopalan, and U. B. Pal, “Polarization measurements on single-step co-fired solid oxide fuel cells (SOFCs),” *J. Power Sources*, vol. 172, no. 1, pp. 39–49, Oct. 2007.
[58] D. . Fagg, J. C. . Abrantes, D. Pérez-Coll, P. Núñez, V. . Kharton, and J. . Frade, “The effect of cobalt oxide sintering aid on electronic transport in Ce0.80Gd0.20O2−δ electrolyte,” *Electrochim. Acta*, vol. 48, no. 8, pp. 1023–1029, Apr. 2003.
[59] J. Mürbe and J. Töpfer, “High permeability Ni–Cu–Zn ferrites through additive-free low-temperature sintering of nanocrystalline powders,” *J. Eur. Ceram. Soc.*, vol. 32, no. 5, pp. 1091–1098, May 2012.
[60] J. Lalande, R. Ollitrault-Fichet, and P. Boch, “Sintering behaviour of CuO-doped SnO2,” *J. Eur. Ceram. Soc.*, vol. 20, no. 14–15, pp. 2415–2420, Dec. 2000.
[61] H. Gao *et al.*, “The effect of Fe doping on the properties of SOFC electrolyte YSZ,” *Solid State Ionics*, vol. 179, no. 27–32, pp. 1620–1624, Sep. 2008.
[62] J. NICHOLAS and L. DEJONGHE, “Prediction and evaluation of sintering aids for Cerium Gadolinium Oxide,” *Solid State Ionics*, vol. 178, no. 19–20, pp. 1187–1194, Jul. 2007.
[63] A. MAI, V. HAANAPPEL, F. TIETZ, and D. STOVER, “Ferrite-based perovskites as cathode materials for anode-supported solid oxide fuel cellsPart II. Influence of the CGO interlayer,” *Solid State Ionics*, vol. 177, no. 19–25, pp. 2103–2107, Oct. 2006.
[64] J. Van Herle and R. Vasquez, “Conductivity of Mn and Ni-doped stabilized zirconia electrolyte,” *J. Eur. Ceram. Soc.*, vol. 24, no. 6, pp. 1177–1180, Jan. 2004.
[65] Z. Sun, E. Fabbri, L. Bi, and E. Traversa, “Lowering grain boundary resistance of

BaZr 0.8 Y 0.2 O 3−δ with LiNO 3 sintering-aid improves proton conductivity for fuel cell operation," *Phys. Chem. Chem. Phys.*, vol. 13, no. 17, pp. 7692–7700, 2011.

[66] T. Zhang *et al.*, "Sintering behavior and ionic conductivity of Ce0.8Gd0.2O1.9 with a small amount of MnO2 doping," *J. Solid State Electrochem.*, vol. 7, no. 6, pp. 348–354, Jun. 2003.

[67] H. Yoshida and T. Inagaki, "Effects of additives on the sintering properties of samaria-doped ceria," *J. Alloys Compd.*, vol. 408–412, pp. 632–636, 2006.

[68] G. C. T. Silva and E. N. S. Muccillo, "Effect of Co Addition on Sintering and Electrical Properties of Yttria-Stabilized Zirconia," in *Sixth International Latin-American Conference on Powder Technology*, vol. 3, pp. 692–697.

[69] A. Mai, V. A. C. Haanappel, F. Tietz, and D. Sto, "Ferrite-based perovskites as cathode materials for anode-supported solid oxide fuel cells Part II . Influence of the CGO interlayer," *Solid State Ionics*, vol. 177, pp. 2103–2107, 2006.

[70] X. Zhou, B. Scarfino, and H. U. Anderson, "Electrical conductivity and stability of Gd-doped ceria / Y-doped zirconia ceramics and thin films," *Solid State Ionics*, vol. 175, pp. 19–22, 2004.

[71] A. Tsoga, A. Gupta, A. Naoumidis, and P. Nikolopoulos, "Gadolinia-doped ceria and yttria stabilized zirconia interfaces: regarding their application for SOFC technology," *Acta Mater.*, vol. 48, pp. 4709–4714, 2000.

[72] D. P. Fagg, A. L. Shaula, V. V Kharton, and J. R. Frade, "High oxygen permeability in Fluorite-type Ce(0.8)Pr(0.2)O(2-d) via the use of sintering aids," *J. Memb. Sci.*, vol. 299, pp. 1–7, 2007.

[73] H. Zhang, H. Liu, Y. Cong, and W. Yang, "Investigation of Sm(0.5)Sr(0.5)CoO(3-d)/Co3O4 composite cathode for intermediate-temperature solid oxide fuel cells," *J. Power*, vol. 185, pp. 129–135, 2008.

[74] D. Chen, C. Huang, R. Ran, H. Jung, C. Kwak, and Z. Shao, "New Ba(0.5)Sr(0.5)Co(0.8)Fe(0.2)O(3-d) + Co3O4 composite electrode for IT-SOFCs with improved electrical conductivity and catalytic activity," *Electrochem. commun.*, vol. 13, no. 2, pp. 197–199, 2011.

[75] A. Mai, V. A. C. Haanappel, S. Uhlenbruck, F. Tietz, and D. Stöver, "Ferrite-based perovskites as cathode materials for anode-supported solid oxide fuel cells: Part I. Variation of composition," *Solid State Ionics*, vol. 176, no. 15–16, pp. 1341–1350, 2005.

[76] D. Chen, F. Wang, and Z. Shao, "Interlayer-free electrodes for IT-SOFCs by applying Co 3O 4 as sintering aid," *Int. J. Hydrogen Energy*, vol. 37, no. 16, pp. 11946–11954, 2012.

[77] L. Niinist, M. Nieminen, J. Pivsaari, J. Niinist, M. Putkonen, and M. Nieminen, "Advanced electronic and optoelectronic materials by Atomic Layer Deposition: An overview with special emphasis on recent progress in processing of high-k dielectrics and other oxide materials," *Phys. status solidi*, vol. 201, no. 7, pp. 1443–1452, May 2004.

[78] M. Knez, K. Nielsch, and L. Niinistö, "Synthesis and Surface Engineering of Complex Nanostructures by Atomic Layer Deposition," *Adv. Mater.*, vol. 19, no. 21, pp. 3425–3438, Nov. 2007.

[79] C. Bernay, A. Ringuedé, P. Colomban, D. Lincot, and M. Cassir, “Yttria-doped zirconia thin films deposited by atomic layer deposition ALD: a structural, morphological and electrical characterisation,” *J. Phys. Chem. Solids*, vol. 64, no. 9–10, pp. 1761–1770, Sep. 2003.
[80] M. Putkonen, T. Sajavaara, J. Niinistö, L.-S. Johansson, and L. Niinistö, “Deposition of yttria-stabilized zirconia thin films by atomic layer epitaxy from β-diketonate and organometallic precursors,” *J. Mater. Chem.*, vol. 12, no. 3, pp. 442–448, Feb. 2002.
[81] M. Putkonen and L. Niinistö, “Zirconia thin films by atomic layer epitaxy. A comparative study on the use of novel precursors with ozone,” *J. Mater. Chem.*, vol. 11, no. 12, pp. 3141–3147, Nov. 2001.
[82] M. Cassir, F. Goubin, C. Bernay, P. Vernoux, and D. Lincot, “Synthesis of ZrO2 thin films by atomic layer deposition: growth kinetics, structural and electrical properties,” *Appl. Surf. Sci.*, vol. 193, no. 1–4, pp. 120–128, Jun. 2002.
[83] J. H. Shim, C.-C. Chao, H. Huang, and F. B. Prinz, “Atomic Layer Deposition of Yttria-Stabilized Zirconia for Solid Oxide Fuel Cells,” *Chem. Mater.*, vol. 19, no. 15, pp. 3850–3854, Jul. 2007.
[84] X. Jiang, H. Huang, F. B. Prinz, and S. F. Bent, “Application of Atomic Layer Deposition of Platinum to Solid Oxide Fuel Cells,” *Chem. Mater.*, vol. 20, no. 12, pp. 3897–3905, Jun. 2008.
[85] R. R. Essex, J. I. Rossero, G. M. Jursich, and C. G. Takoudis, “Atomic Layer Deposition of Cerium Oxide for Potential Use in Solid Oxide Fuel Cells,” *J. Undergrad. Res.*, vol. 6, pp. 37–41, 2013.
[86] Y. Jee *et al.*, “High performance Bi-layered electrolytes via atomic layer deposition for solid oxide fuel cells,” *J. Power Sources*, vol. 253, pp. 114–122, 2014.
[87] C.-C. Chao, C.-M. Hsu, Y. Cui, and F. B. Prinz, “Improved Solid Oxide Fuel Cell Performance with Nanostructured Electrolytes,” *Am. Chem. Soc.*, vol. 5, pp. 5692–5696, 2011.
[88] K. S. Son, K. Bae, and J. W. Kim, “Ion conduction in nanoscale yttria-stabilized zirconia fabricated by atomic layer deposition with various doping rates,” *J. Vac. Sci. Technol.*, vol. 31, 2013.
[89] Y. C. Interlayers, Z. Fan, and F. B. Prinz, “Enhancing Oxide Ion Incorporation Kinetics by Nanoscale Yttria-Doped Ceria Interlayers,” *Nanoletters*, vol. 11, pp. 2202–2205, 2011.
[90] V. KHARTON, F. MARQUES, and A. ATKINSON, “Transport properties of solid oxide electrolyte ceramics: a brief review,” *Solid State Ionics*, vol. 174, no. 1–4, pp. 135–149, Oct. 2004.
[91] J. Päiväsaari, M. Putkonen, and L. Niinistö, “Cerium dioxide buffer layers at low temperature by atomic layer deposition,” *J. Mater. Chem.*, vol. 12, no. 6, pp. 1828–1832, May 2002.
[92] J. Niinistö, N. Petrova, M. Putkonen, L. Niinistö, K. Arstila, and T. Sajavaara, “Gadolinium oxide thin films by atomic layer deposition,” *J. Cryst. Growth*, vol. 285, no. 1–2, pp. 191–200, Nov. 2005.
[93] E. Gourba *et al.*, “Characterisation of thin films of ceria-based electrolytes for

IntermediateTemperature — Solid oxide fuel cells (IT-SOFC)," *Ionics (Kiel).*, vol. 9, no. 1–2, pp. 15–20, Jan. 2003.
[94] E. Ballée, A. Ringuedé, M. Cassir, M. Putkonen, and L. Niinistö, "Synthesis of a Thin-Layered Ionic Conductor, CeO 2 −Y 2 O 3 , by Atomic Layer Deposition in View of Solid Oxide Fuel Cell Applications," *Chem. Mater.*, vol. 21, no. 19, pp. 4614–4619, Oct. 2009.
[95] C. Chao, M. Motoyama, and F. B. Prinz, "Nanostructured Platinum Catalysts by Atomic-Layer Deposition for Solid-Oxide Fuel Cells COMMUNICATION," *Adv. Energy Mater.*, vol. 2, pp. 651–654, 2012.
[96] J. An, Y.-B. Kim, and F. B. Prinz, "Ultra-thin platinum catalytic electrodes fabricated by atomic layer deposition," *Phys. Chem. Chem. Phys.*, vol. 15, pp. 7520–7525, 2013.
[97] X. Jiang, H. Huang, F. B. Prinz, and S. F. Bent, "Application of Atomic Layer Deposition of Platinum to Solid Oxide Fuel Cells," *Chem. Mater.*, no. 10, pp. 3897–3905, 2008.
[98] T. P. Holme, C. Lee, and F. B. Prinz, "Atomic layer deposition of LSM cathodes for solid oxide fuel cells," *Solid State Ionics*, vol. 179, pp. 1540–1544, 2008.
[99] M. Nieminen, M. Putkonen, and L. Niinistö, "Formation and stability of lanthanum oxide thin films deposited from β-diketonate precursor," *Appl. Surf. Sci.*, vol. 174, no. 2, pp. 155–166, Apr. 2001.
[100] T. P. Holme, C. Lee, and F. B. Prinz, "Atomic layer deposition of LSM cathodes for solid oxide fuel cells," *Solid State Ionics*, vol. 179, no. 27–32, pp. 1540–1544, Sep. 2008.
[101] O. Nilsen, E. Rauwel, H. Fjellvåg, and A. Kjekshus, "Growth of La 1−x CaxMnO 3 thin films by atomic layer deposition," *J. Mater. Chem.*, vol. 17, no. 15, pp. 1466–1475, 2007.
[102] B. J. M. Vohs and R. J. Gorte, "High-Performance SOFC Cathodes Prepared by Infiltration," *Adv. Mater.*, pp. 943–956, 2009.
[103] S. B. Adler, "Factors Governing Oxygen Reduction in Solid Oxide Fuel Cell Cathodes †," 2004.
[104] R. Küngas, F. Bidrawn, E. Mahmoud, J. M. Vohs, and R. J. Gorte, "Evidence of surface-reaction rate limitations in SOFC composite cathodes," *Solid State Ionics*, vol. 225, pp. 146–150, 2012.
[105] F. Bidrawn, R. Ku, J. M. Vohs, and R. J. Gorte, "Modeling Impedance Response of SOFC Cathodes Prepared by Infiltration," *J. Electrochem. Soc.*, vol. 158, no. 5, pp. 514–525, 2011.
[106] F. Bidrawn, G. Kim, N. Aramrueang, J. M. Vohs, and R. J. Gorte, "Dopants to enhance SOFC cathodes based on Sr-doped LaFeO 3 and LaMnO 3," *J. Power Sources*, vol. 195, pp. 720–728, 2010.
[107] Y. Gong *et al.*, "Stabilizing Nanostructured Solid Oxide Fuel Cell Cathode with Atomic Layer Deposition," *Nanoletters*, vol. 13, pp. 4340–4345, 2013.
[108] M. Rahmanipour, Y. Cheng, T. M. Onn, A. Donazzi, and J. M. Vohs, "Modification of LSF-YSZ Composite Cathodes by Atomic Layer," *J. Electrochem. Soc.*, vol. 164, no. 7, pp. F879–F884, 2017.
[109] A. S. Yu, K. Rainer, J. M. Vohs, and R. J. Gorte, "Modification of SOFC Cathodes

by Atomic Layer Deposition," *J. Electrochem. Soc.*, vol. 160, no. 11, pp. 1225–1231, 2013.
[110] Y. Gong *et al.*, "Atomic Layer Deposition Functionalized Composite SOFC Cathode La(0.6)Sr(0.4)Fe(0.8)Co(0.2)-Gd(0.2)Ce(0.8)O(1.9): Enhanced Long-Term Stability," *Chem. Mater.*, vol. 25, pp. 4224–4231, 2013.
[111] T. Z. Sholklapper, H. Kurokawa, C. P. Jacobson, and S. J. Visco, "Nanostructured Solid Oxide Fuel Cell Electrodes," *Nanoletters*, vol. 7, no. 7, pp. 2136–2141, 2007.
[112] S. B. Adler, "Factors governing oxygen reduction in solid oxide fuel cell cathodes," *Chem. Rev.*, vol. 104, no. 10, pp. 4791–4843, 2004.
[113] A. J. Jacobson, "Materials for Solid Oxide Fuel Cells †," *Chem. Mater.*, vol. 22, no. 3, pp. 660–674, Feb. 2010.
[114] B. C. H. Steele and A. Heinzel, "Materials for fuel-cell technologies," *Nature*, vol. 414, no. 6861, pp. 345–352, Nov. 2001.
[115] D. Ding, X. Li, S. Y. Lai, K. Gerdes, and M. Liu, "Enhancing SOFC cathode performance by surface modification through infiltration," *Energy Environ. Sci.*, vol. 7, no. 2, p. 552, 2014.
[116] T. Hibino, "A Low-Operating-Temperature Solid Oxide Fuel Cell in Hydrocarbon-Air Mixtures," *Science (80-.).*, vol. 288, no. 5473, pp. 2031–2033, Jun. 2000.
[117] E. D. Wachsman and K. T. Lee, "Lowering the Temperature of Solid Oxide Fuel Cells," *Science (80-.).*, vol. 334, no. 6058, pp. 935–939, Nov. 2011.
[118] E.-O. Oh *et al.*, "Extremely Thin Bilayer Electrolyte for Solid Oxide Fuel Cells (SOFCs) Fabricated by Chemical Solution Deposition (CSD)," *Adv. Mater.*, vol. 24, no. 25, pp. 3373–3377, Jul. 2012.
[119] Z. Shao and S. M. Haile, "A high-performance cathode for the next generation of solid-oxide fuel cells," *Nature*, vol. 431, no. 7005, pp. 170–173, Sep. 2004.
[120] A. Evans *et al.*, "Micro-solid oxide fuel cells: status, challenges, and chances," *Monatshefte für Chemie - Chem. Mon.*, vol. 140, no. 9, pp. 975–983, Sep. 2009.
[121] G. Wu, K. L. More, C. M. Johnston, and P. Zelenay, "High-Performance Electrocatalysts for Oxygen Reduction Derived from Polyaniline, Iron, and Cobalt," *Science (80-.).*, vol. 332, no. 6028, pp. 443–447, Apr. 2011.
[122] M. Cargnello *et al.*, "Exceptional Activity for Methane Combustion over Modular Pd@CeO2 Subunits on Functionalized Al2O3," *Science (80-.).*, vol. 337, no. 6095, pp. 713–717, Aug. 2012.
[123] F. Gao and D. W. Goodman, "Model Catalysts: Simulating the Complexities of Heterogeneous Catalysts," *Annu. Rev. Phys. Chem.*, vol. 63, no. 1, pp. 265–286, May 2012.
[124] F. Boccuzzi, A. Chiorino, and M. Manzoli, "Au/TiO2 nanostructured catalyst: effects of gold particle sizes on CO oxidation at 90 K," *Mater. Sci. Eng. C*, vol. 15, no. 1–2, pp. 215–217, Aug. 2001.
[125] I. Balint, A. Miyazaki, and K. Aika, "Investigation of the morphology–catalytic reactivity relationship for Pt nanoparticles supported on alumina by using the reduction of NO with CH4 as a model reaction," *Chem. Commun.*, no. 10, pp. 1044–1045, May 2002.
[126] X. Feng *et al.*, "Synthesis and deposition of ultrafine Pt nanoparticles within high

aspect ratio TiO2 nanotube arrays: application to the photocatalytic reduction of carbon dioxide," *J. Mater. Chem.*, vol. 21, no. 35, p. 13429, 2011.
[127] H.-J. Freund and G. Pacchioni, "Oxide ultra-thin films on metals: new materials for the design of supported metal catalysts," *Chem. Soc. Rev.*, vol. 37, no. 10, p. 2224, 2008.
[128] L. Adijanto *et al.*, "Synthesis and Stability of Pd@CeO 2 Core–Shell Catalyst Films in Solid Oxide Fuel Cell Anodes," *ACS Catal.*, vol. 3, no. 8, pp. 1801–1809, Aug. 2013.
[129] S. H. Joo, J. Y. Park, C.-K. Tsung, Y. Yamada, P. Yang, and G. A. Somorjai, "Thermally stable Pt/mesoporous silica core–shell nanocatalysts for high-temperature reactions," *Nat. Mater.*, vol. 8, no. 2, pp. 126–131, Feb. 2009.
[130] P. M. Arnal, M. Comotti, and F. Schüth, "High-Temperature-Stable Catalysts by Hollow Sphere Encapsulation," *Angew. Chemie Int. Ed.*, vol. 45, no. 48, pp. 8224–8227, Dec. 2006.
[131] M. Seipenbusch and A. Binder, "Structural Stabilization of Metal Nanoparticles by Chemical Vapor Deposition-Applied Silica Coatings," *J. Phys. Chem. C*, vol. 113, no. 48, pp. 20606–20610, Dec. 2009.
[132] B. J. O'Neill *et al.*, "Catalyst Design with Atomic Layer Deposition," *ACS Catal.*, vol. 5, no. 3, pp. 1804–1825, Mar. 2015.
[133] I. Chang, S. Ji, J. Park, M. H. Lee, and S. W. Cha, "Ultrathin YSZ Coating on Pt Cathode for High Thermal Stability and Enhanced Oxygen Reduction Reaction Activity," *Adv. Energy Mater.*, vol. 5, no. 10, May 2015.
[134] Y. K. Li *et al.*, "Nanoporous silver cathodes surface-treated by atomic layer deposition of Y:ZrO2 for high-performance low-temperature solid oxide fuel cells," *J. Power Sources*, vol. 295, pp. 175–181, Nov. 2015.
[135] K.-Y. Liu, L. Fan, C.-C. Yu, and P.-C. Su, "Thermal stability and performance enhancement of nano-porous platinum cathode in solid oxide fuel cells by nanoscale ZrO2 capping," *Electrochem. commun.*, vol. 56, pp. 65–69, Jul. 2015.
[136] Y. Takeda, "Cathodic Polarization Phenomena of Perovskite Oxide Electrodes with Stabilized Zirconia," *J. Electrochem. Soc.*, vol. 134, no. 11, p. 2656, 1987.
[137] M. J. Escudero, A. Aguadero, J. A. Alonso, and L. Daza, "A kinetic study of oxygen reduction reaction on La2NiO4 cathodes by means of impedance spectroscopy," *J. Electroanal. Chem.*, vol. 611, no. 1–2, pp. 107–116, Dec. 2007.
[138] J. H. Shim, J. S. Park, J. An, T. M. Gür, S. Kang, and F. B. Prinz, "Intermediate-Temperature Ceramic Fuel Cells with Thin Film Yttrium-Doped Barium Zirconate Electrolytes," *Chem. Mater.*, vol. 21, no. 14, pp. 3290–3296, Jul. 2009.
[139] Z. Fan and F. B. Prinz, "Enhancing Oxide Ion Incorporation Kinetics by Nanoscale Yttria-Doped Ceria Interlayers," *Nano Lett.*, vol. 11, no. 6, pp. 2202–2205, Jun. 2011.
[140] T. Hibino, A. Hashimoto, M. Suzuki, and M. Sano, "A Solid Oxide Fuel Cell Using Y-Doped BaCeO[sub 3] with Pd-Loaded FeO Anode and Ba[sub 0.5]Pr[sub 0.5]CoO[sub 3] Cathode at Low Temperatures," *J. Electrochem. Soc.*, vol. 149, no. 11, p. A1503, 2002.
[141] N. V. Lyskov, M. S. Kaluzhskikh, L. S. Leonova, G. N. Mazo, S. Y. Istomin, and E. V. Antipov, "Electrochemical characterization of Pr2CuO4 cathode for IT-

SOFC," *Int. J. Hydrogen Energy*, vol. 37, no. 23, pp. 18357–18364, Dec. 2012.
[142] F. B. O'Hayre, R. P.; Cha, S.-W.; Colella, W. G.; Prinz, *Fuel Cell Fundamentals, 2nd ed.* John Wiley Sons, 2009.
[143] Y. Gong, X. Li, L. Zhang, W. Tharp, C. Qin, and K. Huang, "Promoting Electrocatalytic Activity of a Composite SOFC Cathode La0.8Sr0.2MnO3+ /Ce0.8Gd0.2O2- with Molten Carbonates," *J. Electrochem. Soc.*, vol. 161, no. 3, pp. F226–F232, Dec. 2013.
[144] A. Weber and E. Ivers-Tiffée, "Materials and concepts for solid oxide fuel cells (SOFCs) in stationary and mobile applications," *J. Power Sources*, vol. 127, no. 1–2, pp. 273–283, Mar. 2004.
[145] Z. Gao, L. V. Mogni, E. C. Miller, J. G. Railsback, and S. A. Barnett, "A perspective on low-temperature solid oxide fuel cells," *Energy Environ. Sci.*, vol. 9, no. 5, pp. 1602–1644, 2016.
[146] D. J. L. Brett, A. Atkinson, N. P. Brandon, and S. J. Skinner, "Intermediate temperature solid oxide fuel cells.," *Chem. Soc. Rev.*, vol. 37, no. 8, pp. 1568–78, Aug. 2008.
[147] M. C. Tucker, "Progress in metal-supported solid oxide fuel cells: A review," *J. Power Sources*, vol. 195, no. 15, pp. 4570–4582, Aug. 2010.
[148] S. Ji *et al.*, "Substrate-dependent growth of nanothin film solid oxide fuel cells toward cost-effective nanostructuring," *Int. J. Precis. Eng. Manuf. Technol.*, vol. 3, no. 1, pp. 35–39, Jan. 2016.
[149] D. Gostovic, J. R. Smith, D. P. Kundinger, K. S. Jones, and E. D. Wachsman, "Three-Dimensional Reconstruction of Porous LSCF Cathodes," *Electrochem. Solid-State Lett.*, vol. 10, no. 12, p. B214, 2007.
[150] P. Leone, M. Santarelli, P. Asinari, M. Calì, and R. Borchiellini, "Experimental investigations of the microscopic features and polarization limiting factors of planar SOFCs with LSM and LSCF cathodes," *J. Power Sources*, vol. 177, no. 1, pp. 111–122, Feb. 2008.
[151] E. Perry Murray, "Electrochemical performance of (La,Sr)(Co,Fe)O3–(Ce,Gd)O3 composite cathodes," *Solid State Ionics*, vol. 148, no. 1–2, pp. 27–34, May 2002.
[152] B. Steele, "Properties of La0.6Sr0.4Co0.2Fe0.8O3−x (LSCF) double layer cathodes on gadolinium-doped cerium oxide (CGO) electrolytes II. Role of oxygen exchange and diffusion," *Solid State Ionics*, vol. 106, no. 3–4, pp. 255–261, 1998.
[153] E. N. Armstrong, K. L. Duncan, D. J. Oh, J. F. Weaver, and E. D. Wachsman, "Determination of Surface Exchange Coefficients of LSM, LSCF, YSZ, GDC Constituent Materials in Composite SOFC Cathodes," *J. Electrochem. Soc.*, vol. 158, no. 5, p. B492, 2011.
[154] W. Yu *et al.*, "Performance enhancement of thin film LSCF cathodes by gold current collecting layer," *Int. J. Precis. Eng. Manuf. Technol.*, vol. 3, no. 2, pp. 185–188, Apr. 2016.
[155] Y. LENG, S. CHAN, and Q. LIU, "Development of LSCF–GDC composite cathodes for low-temperature solid oxide fuel cells with thin film GDC electrolyte," *Int. J. Hydrogen Energy*, vol. 33, no. 14, pp. 3808–3817, Jul. 2008.
[156] H. Choi, G. Y. Cho, and S.-W. Cha, "Fabrication and characterization of anode supported YSZ/GDC bilayer electrolyte SOFC using dry press process," *Int. J.*

Precis. Eng. Manuf. Technol., vol. 1, no. 2, pp. 95–99, Apr. 2014.
[157] F. Qiang, K. Sun, N. Zhang, S. Le, X. Zhu, and J. Piao, "Optimization on fabrication and performance of A-site-deficient La0.58Sr0.4Co0.2Fe0.8O3-δ cathode for SOFC," *J. Solid State Electrochem.*, vol. 13, no. 3, pp. 455–467, Mar. 2009.
[158] S. P. Jiang, "Issues on development of (La,Sr)MnO3 cathode for solid oxide fuel cells," *J. Power Sources*, vol. 124, no. 2, pp. 390–402, 2003.
[159] Y. Gong, W. Ji, L. Zhang, B. Xie, and H. Wang, "Performance of (La,Sr)MnO3 cathode based solid oxide fuel cells: Effect of bismuth oxide sintering aid in silver paste cathode current collector," *J. Power Sources*, vol. 196, no. 3, pp. 928–934, 2011.
[160] W. Liu, Z. Zhao, B. Tu, D. Cui, D. Ou, and M. Cheng, "TiO2-modified La0.6Sr0.4Co0.2Fe0.8O3-δ cathode for intermediate temperature solid oxide fuel cells," *Chinese J. Catal.*, vol. 36, no. 4, pp. 502–508, 2015.
[161] D. Chen, F. Wang, and Z. Shao, "Interlayer-free electrodes for IT-SOFCs by applying Co3O4 as sintering aid," *Int. J. Hydrogen Energy*, vol. 37, no. 16, pp. 11946–11954, Aug. 2012.
[162] V. Dusastre and J. A. Kilner, "Optimisation of composite cathodes for intermediate temperature SOFC applications," *Solid State Ionics*, vol. 126, no. 1, pp. 163–174, 1999.
[163] C. M. Kleinlogel, "Mixed Electronic-Ionic Conductivity of Cobalt Doped Cerium Gadolinium Oxide," *J. Electroceramics*, vol. 5, no. 3, pp. 231–243, 2000.
[164] X. Qi, Y. S. Lin, and S. L. Swartz, "Electric Transport and Oxygen Permeation Properties of Lanthanum Cobaltite Membranes Synthesized by Different Methods," *Ind. Eng. Chem. Res.*, vol. 39, no. 3, pp. 646–653, Mar. 2000.
[165] J. W. Stevenson, "Electrochemical Properties of Mixed Conducting Perovskites La[sub 1−x]M[sub x]Co[sub 1−y]Fe[sub y]O[sub 3−δ] (M = Sr, Ba, Ca)," *J. Electrochem. Soc.*, vol. 143, no. 9, p. 2722, 1996.
[166] H. Zhang and W. Yang, "Highly efficient electrocatalysts for oxygen reduction reaction," *Chem. Commun.*, no. 41, p. 4215, 2007.
[167] A. Gaur and V. M. Sglavo, "Flash Sintering of (La, Sr)(Co, Fe)O 3 -Gd-Doped CeO 2 Composite," *J. Am. Ceram. Soc.*, vol. 98, no. 6, pp. 1747–1752, Jun. 2015.
[168] L. Navarrete, C. Solís, and J. M. Serra, "Boosting the oxygen reduction reaction mechanisms in IT-SOFC cathodes by catalytic functionalization," *J. Mater. Chem. A*, vol. 3, no. 32, pp. 16440–16444, 2015.
[169] N. Hildenbrand, B. A. Boukamp, P. Nammensma, and D. H. A. Blank, "Improved cathode/electrolyte interface of SOFC," *Solid State Ionics*, vol. 192, no. 1, pp. 12–15, Jun. 2011.
[170] K. T. Lee, D. W. Jung, H. S. Yoon, A. A. Lidie, M. A. Camaratta, and E. D. Wachsman, "Interfacial modification of La0.80Sr0.20MnO3−δ–Er0.4Bi0.6O3 cathodes for high performance lower temperature solid oxide fuel cells," *J. Power Sources*, vol. 220, pp. 324–330, Dec. 2012.
[171] S. Molin, A. Chrzan, J. Karczewski, D. Szymczewska, and P. Jasinski, "THE ROLE OF THIN FUNCTIONAL LAYERS IN SOLID OXIDE FUEL CELLS," *Electrochim. Acta*, vol. 204, pp. 136–145, Jun. 2016.

[172] S. Molin and P. Z. Jasinski, “Improved performance of LaNi0.6Fe0.4O3 solid oxide fuel cell cathode by application of a thin interface cathode functional layer,” *Mater. Lett.*, vol. 189, pp. 252–255, Feb. 2017.
[173] A. Chrzan, J. Karczewski, M. Gazda, D. Szymczewska, and P. Jasinski, “Investigation of thin perovskite layers between cathode and doped ceria used as buffer layer in solid oxide fuel cells,” *J. Solid State Electrochem.*, vol. 19, no. 6, pp. 1807–1815, Jun. 2015.
[174] A. Chrzan, J. Karczewski, D. Szymczewska, and P. Jasinski, “Nanocrystalline cathode functional layer for SOFC,” *Electrochim. Acta*, vol. 225, pp. 168–174, Jan. 2017.
[175] A. Evans *et al.*, “Integration of Spin-Coated Nanoparticulate-Based La 0.6 Sr 0.4 CoO 3-δ Cathodes into Micro-Solid Oxide Fuel Cell Membranes,” *Fuel Cells*, vol. 13, no. 3, pp. 441–444, Jun. 2013.
[176] K. Zhao, Q. Xu, D.-P. Huang, M. Chen, and B.-H. Kim, “Microstructure and electrochemical properties of porous La2NiO4+δ electrodes spin-coated on Ce0.8Sm0.2O1.9 electrolyte,” *Ionics (Kiel).*, vol. 18, no. 1–2, pp. 75–83, Jan. 2012.
[177] L. Baqué, K. P. Padmasree, M. A. Ceniceros Reyes, H. Troiani, A. Serquis, and A. Soldati, “Improved Sr 0.6 La 0.4 Co 0.8 Fe 0.2 O 3−δ /Ce 0.8 Y 0.2 O 2−δ interface for IT-SOFC applications,” *Int. J. Hydrogen Energy*, vol. 41, no. 3, pp. 1958–1965, Jan. 2016.
[178] B. Huang, X. Zhu, H. Nie, Y. Niu, Y. Li, and N. Cheng, “Comparison of the electrochemical properties of impregnated and functionally gradient LaNi0.6Fe0.4O3–Gd0.2Ce0.8O2 composite cathodes for Solid Oxide Fuel Cell,” *J. Power Sources*, vol. 235, pp. 20–28, Aug. 2013.
[179] N. Hildenbrand, B. A. Boukamp, P. Nammensma, and D. H. A. Blank, “Improved cathode/electrolyte interface of SOFC,” *Solid State Ionics*, vol. 192, no. 1, pp. 12–15, Jun. 2011.
[180] X. Zhang, S. H. Chan, G. Li, H. K. Ho, J. Li, and Z. Feng, “A review of integration strategies for solid oxide fuel cells,” *J. Power Sources*, vol. 195, no. 3, pp. 685–702, Feb. 2010.
[181] Y. Zhao *et al.*, “Recent progress on solid oxide fuel cell: Lowering temperature and utilizing non-hydrogen fuels,” *Int. J. Hydrogen Energy*, vol. 38, no. 36, pp. 16498–16517, Dec. 2013.
[182] E. Ivers-Tiffée, A. Weber, and D. Herbstritt, “Materials and technologies for SOFC-components,” *J. Eur. Ceram. Soc.*, vol. 21, no. 10–11, pp. 1805–1811, Jan. 2001.
[183] E. V. Tsipis and V. V. Kharton, “Electrode materials and reaction mechanisms in solid oxide fuel cells: a brief review,” *J. Solid State Electrochem.*, vol. 12, no. 9, pp. 1039–1060, Sep. 2008.
[184] R. Barfod, A. Hagen, S. Ramousse, P. V. Hendriksen, and M. Mogensen, “Break Down of Losses in Thin Electrolyte SOFCs,” *Fuel Cells*, vol. 6, no. 2, pp. 141–145, Apr. 2006.
[185] E. V. Tsipis and V. V. Kharton, “Electrode materials and reaction mechanisms in

solid oxide fuel cells: a brief review," *J. Solid State Electrochem.*, vol. 12, no. 11, pp. 1367–1391, Nov. 2008.
[186] E. V. Tsipis and V. V. Kharton, "Electrode materials and reaction mechanisms in solid oxide fuel cells: a brief review. III. Recent trends and selected methodological aspects," *J. Solid State Electrochem.*, vol. 15, no. 5, pp. 1007–1040, May 2011.
[187] S. B. Adler, "Factors Governing Oxygen Reduction in Solid Oxide Fuel Cell Cathodes †," *Chem. Rev.*, vol. 104, no. 10, pp. 4791–4844, Oct. 2004.
[188] C. F. Setevich, L. V. Mogni, A. Caneiro, and F. D. Prado, "Optimum cathode configuration for IT-SOFC using La0.4Ba0.6CoO3−δ and Ce0.9Gd0.1O1.95," *Int. J. Hydrogen Energy*, vol. 37, no. 19, pp. 14895–14901, Oct. 2012.
[189] J. McCoppin, D. Young, T. Reitz, A. Maleszewski, and S. Mukhopadhyay, "Solid oxide fuel cell with compositionally graded cathode functional layer deposited by pressure assisted dual-suspension spraying," *J. Power Sources*, vol. 196, no. 8, pp. 3761–3765, Apr. 2011.
[190] V. A. C. Haanappel *et al.*, "Advances in Research, Development, and Testing of Single Cells at Forschungszentrum Jülich," *J. Fuel Cell Sci. Technol.*, vol. 6, no. 2, May 2009.
[191] C. W. Tanner, "The Effect of Porous Composite Electrode Structure on Solid Oxide Fuel Cell Performance," *J. Electrochem. Soc.*, vol. 144, no. 1, p. 21, 1997.
[192] M. Rieu, R. Sayers, M. A. Laguna-Bercero, S. J. Skinner, P. Lenormand, and F. Ansart, "Investigation of Graded La[sub 2]NiO[sub 4+δ] Cathodes to Improve SOFC Electrochemical Performance," *J. Electrochem. Soc.*, vol. 157, no. 4, p. B477, 2010.
[193] R. J. Woolley and S. J. Skinner, "Functionally graded composite La 2 NiO 4+δ and La 4 Ni 3 O 10−δ solid oxide fuel cell cathodes," *Solid State Ionics*, vol. 255, pp. 1–5, Feb. 2014.
[194] K. T. Lee, D. W. Jung, H. S. Yoon, A. A. Lidie, M. A. Camaratta, and E. D. Wachsman, "Interfacial modification of La0.80Sr0.20MnO3−δ–Er0.4Bi0.6O3 cathodes for high performance lower temperature solid oxide fuel cells," *J. Power Sources*, vol. 220, pp. 324–330, Dec. 2012.
[195] A. Chrzan, J. Karczewski, M. Gazda, D. Szymczewska, and P. Jasinski, "Investigation of thin perovskite layers between cathode and doped ceria used as buffer layer in solid oxide fuel cells," *J. Solid State Electrochem.*, vol. 19, no. 6, pp. 1807–1815, Jun. 2015.
[196] A. Evans *et al.*, "Integration of Spin-Coated Nanoparticulate-Based La 0.6 Sr 0.4 CoO 3-δ Cathodes into Micro-Solid Oxide Fuel Cell Membranes," *Fuel Cells*, vol. 13, no. 3, pp. 441–444, Jun. 2013.
[197] K. Zhao, Q. Xu, D.-P. Huang, M. Chen, and B.-H. Kim, "Microstructure and electrochemical properties of porous La2NiO4+δ electrodes spin-coated on Ce0.8Sm0.2O1.9 electrolyte," *Ionics (Kiel).*, vol. 18, no. 1–2, pp. 75–83, Jan. 2012.
[198] A. Giuliano, C. Nicollet, S. Fourcade, F. Mauvy, M. P. Carpanese, and J.-C. Grenier, "Influence of the electrode/electrolyte interface structure on the performance of Pr 0.8 Sr 0.2 Fe 0.7 Ni 0.3 O 3-δ as Solid Oxide Fuel Cell

cathode," *Electrochim. Acta*, vol. 236, pp. 328–336, May 2017.
[199] S. Molin, A. Chrzan, J. Karczewski, D. Szymczewska, and P. Jasinski, "THE ROLE OF THIN FUNCTIONAL LAYERS IN SOLID OXIDE FUEL CELLS," *Electrochim. Acta*, vol. 204, pp. 136–145, Jun. 2016.
[200] S. Molin and P. Z. Jasinski, "Improved performance of LaNi0.6Fe0.4O3 solid oxide fuel cell cathode by application of a thin interface cathode functional layer," *Mater. Lett.*, vol. 189, pp. 252–255, Feb. 2017.
[201] L. Baqué, K. P. Padmasree, M. A. Ceniceros Reyes, H. Troiani, A. Serquis, and A. Soldati, "Improved Sr 0.6 La 0.4 Co 0.8 Fe 0.2 O 3−δ /Ce 0.8 Y 0.2 O 2−δ interface for IT-SOFC applications," *Int. J. Hydrogen Energy*, vol. 41, no. 3, pp. 1958–1965, Jan. 2016.